

GLOBAL DISTRIBUTION OF DEEP CONVECTION REACHING TROPOPAUSE

A Thesis

by

NANA LIU

BS, Lanzhou University, China, 2013

Submitted in Partial Fulfillment of the Requirements for the Degree of

MASTER of SCIENCE

in

ENVIRONMENTAL SCIENCE

Texas A&M University-Corpus Christi
Corpus Christi, Texas

August 2016

© Nana Liu
All Rights Reserved
August 2016

GLOBAL DISTRIBUTION OF DEEP CONVECTION REACHING TROPOPAUSE

A Thesis

by

NANA LIU

This thesis meets the standards for scope and quality of
Texas A&M University-Corpus Christi and is hereby approved.

Chuntao Liu, PhD
Chair

Feiqin Xie, PhD
Committee Member

Toshiaki Shinoda, PhD
Committee Member

August 2016

ABSTRACT

Correct description of stratosphere-troposphere exchange process is important in the prediction of global climate change. In the process, convection may vertically transport tropospheric air and chemical species into the stratosphere through rapid injection of air. Therefore, it is critical to understand the geo-graphical distribution and characteristic of deep convection reaching tropopause globally.

To characterize and quantify tropopause-reaching deep convection, one-year Global Precipitation Mission (GPM) Ku-band radar echoes were surveyed in relation to several reference levels that are determined by the near-coincident ERA-Interim reanalysis dataset. First, the Precipitation Features were defined by grouping the contiguous areas with non-zero near surface precipitation using Ku band radar. Then the maximum height with detectable radar reflectivity were used as proxies of the top of storms. The deep convections were considered in this study reaching six different reference levels.

Consistent with the observations of the Tropical Rainfall Measuring Mission (TRMM) over the tropics, the GPM has detected tropopause-reaching deep convection dominantly over tropical land, especially over Panama and Central Africa. At mid and high latitudes, tropopause-reaching convective storms are mainly found over land in the Northern Hemisphere during the summer. Compared to those in the tropics, convective cores at mid and high latitudes have relatively larger sizes near the tropopause, especially those over central North America. The meridional distributions of the occurrences of 15 dBZ and 20 dBZ radar echoes at the tropopause

show two comparable maxima, one in the tropics and the other in northern mid-high latitudes. This implies that the convection penetrating the tropopause at northern mid-high latitudes is as frequent as those over the tropics. During boreal summer, such mid-high latitude storm occurrence is even greater than that in the tropics.

The properties of Overshooting Precipitation Features (OPFs) in different region were also investigated. The OPFs above the cold point tropopause height (Z_{CP}) and Z_{380K} over land in the subtropics are even stronger than those in the tropics.

Though one-year GPM observations have shown a global distribution of deep convective storms with updrafts of sufficient strength to penetrate the tropopause and even into the “overworld”, it is still difficult to quantify the vertical transport of trace gases into the stratosphere associated with these storms.

The definition of tropopause heights and the unknown detrainment processes at these altitudes still remain challenges in understanding the mechanism of overshooting convection in the troposphere and stratosphere exchanges. More observations and research about tropopause-reaching deep convection are necessary to understand the vertical transport of trace gases between the troposphere and the stratosphere.

ACKNOWLEDGMENTS

I would like to thank Dr. Chuntao Liu for his invaluable assistance and insights leading to the writing of my thesis. My sincere thanks also goes to the other two members of my graduate committee for their patience and understanding during the one years of effort that went into the production of this research work. Also thanks to Dr. Laura Pan at NCAR for her valuable suggestions that significantly improved the quality of the journal publications based on this work.

This research was supported by NASA Precipitation Measurement Mission grants NNX11AG31G under the direction of Dr. Ramesh Kakar. Thanks also go to Dr. Erich Stocker and Patty McCaughey and the rest of the Precipitation Processing System (PPS) team at NASA Goddard Space Flight Center, Greenbelt, MD, for data processing assistance. ERA-Interim data are obtained from <http://apps.ecmwf.int/datasets/data/interim-full-dai>

TABLE OF CONTENTS

CONTENTS	PAGE
ABSTRACT.....	V
ACKNOWLEDGMENTS	VII
TABLE OF CONTENTS	VIII
LIST OF FIGURES	X
LIST OF TABLES	XIII
1. INTRODUCTION	1
2. DATA AND METHOD.....	5
3. RESULTS.....	11
3.1 Geographical distribution of OPFs	12
3.2 Seasonal variation of zonal mean distribution of OPFs.....	18
3.3 Diurnal Variation of OPFs	21
3.4 Vertical structure of OPFs.....	22
3.5 Large scale environments of OPFs	24
3.6 Linkage between high water vapor values in the low stratosphere and deep convection..	25
3. 7 Uncertainties and implications to the convective vertical transports.....	26

4. SUMMARY	27
REFERENCE.....	29
APPENDIX.....	36
TABLES.....	37
FIGURES	40

LIST OF FIGURES

FIGURES	PAGE
<p>Figure 1. An example of deep convection reaching above tropopause over Nebraska, United States.</p> <p style="padding-left: 40px;">Color fill is the Ku radar reflectivity. The dotted, dashed and solid lines are GPM Microwave Imager (GMI) brightness temperatures at 183 ± 7, 37 and 89 GHz. The lapse rate tropopause height derived from ERA-Interim is 13.3 km. The area with 20 dBZ at 13.3 km in this storm is 2750 km²</p>	40
<p>Figure 2. Two dimensional histogram of various reference levels at different latitudes derived from ERA-Interim reanalysis for PFs. (a) Level of Neutral Buoyancy (Z_{LNB}). (b) Height with potential temperature at 380 K (Z_{380K}), (c) Lapse Rate Tropopause (Z_{LRT}). (d) The Coldest Point (Z_{CP}). (e) Height with Potential Vorticity Unit at 2 (Z_{PV}). (f) Two dimensional histogram of maximal 20 dBZ echo top heights in PFs. The mean Z_{LRT}, Z_{CP}, Z_{380K}, Z_{PV} and Z_{LNB} are overlaid.</p>	41
<p>Figure 3. Locations of OPFs identified with different reference levels. (a) 14 km, (b) Z_{LNB}, (c) Z_{LRT}, (d) Z_{CP}, (e) Z_{PV}, and (f) Z_{380K}. The PFs categorized by the overshooting distance above the reference levels are shown in symbols of different colors.</p>	42
<p>Figure 4. Histogram of various reference levels when OPFs occur in different latitude zones. (a) 40°N-60°N. (b) 20°N-40°N. (c) 20°S-20°N. (d) 20°S-40°S. (e) 40°S-60°S.</p>	43
<p>Figure 5. Maximum 20 dBZ echo top heights (red dots) of OPFs reaching above Z_{CP}. The reference levels Z_{CP} are shown with black dots. Z_{LRT} are shown with gray dots. (a) 40°N-60°N. (b) 20°N-40°N. (c) 20°S-20°N. (d) 20°S-40°S.</p>	46

Figure 6. Global distribution of area of 20 dBZ in OPFs at different reference levels. (a) Z_{LRT} , (b) Z_{CP} , (c) Z_{PV} , and (d) Z_{380K} 45

Figure 7. Global distribution of occurrence of 20 dBZ at different reference levels. (a) 14 km, (b) Z_{LRT} , (c) Z_{CP} , (d) Z_{PV} , and (e) Z_{380K} . The occurrences are calculated by dividing total number of pixels with 20 dBZ at reference levels with total number of sampled pixels in each $5^\circ \times 5^\circ$ box..... 46

Figure 8. (a) Zonal distribution of populations of OPFs with 20 dBZ at Z_{LRT} . (b) Zonal mean area of 20 dBZ at Z_{LRT} per OPF. (c) Zonal mean occurrence of 20 dBZ at Z_{LRT} . The occurrence in each 5° zones are calculated by dividing 20 dBZ pixels at tropopause with total sampled pixels..... 49

Figure 9. Same as Figure 8, but using Z_{CP} as the reference height..... 50

Figure 10. Same as Figure 8, but using Z_{380K} as the reference height. 51

Figure 11. Contribution of areas of 20 and 15 dBZ at Z_{LRT} , Z_{CP} , and Z_{380K} (in units %) in different seasons and latitudes after considering the Earth surface area at each latitude bin. Total values in each panel add up to 100%..... 50

Figure 12. Diurnal variation of population of overshooting precipitation features defined with different reference heights over land (red) and ocean (blue). (a) over $20^\circ S$ - $20^\circ N$. (b) over $20^\circ S$ - $40^\circ S$ and $20^\circ N$ - $40^\circ N$. (c) over $40^\circ S$ - $65^\circ S$ and $40^\circ N$ - $65^\circ N$ 51

Figure 13. Mean profiles of maximum reflectivity (dBZ) for OPFs above different reference heights in different regions. (a) above Z_{LRT} , (b) above Z_{CP} , (c) above Z_{380K} . The tropics are defined from $20^\circ S$ - $20^\circ N$; the subtropics are from 20 - 40° ; the midhigh are defined from

40-60 °; the region for US is 25-60 °N and 60-120 °W; the region for Russia is 40-60 ° N and 0-135 ° E.....	52
Figure 14. Mean area of 20 dBZ for OPFs above different reference heights in different regions. The region is the same as Figure 13.....	53
Figure 15. Mean area of 30 dBZ for OPFs above different reference heights in different regions.....	54
Figure 16. Mean area of 40 dBZ for OPFs above different reference heights in different regions.....	57
Figure 17. Global distribution of mean CAPE in OPFs at different reference levels. (a) Z_{LRT} , (b) Z_{CP} , and (c) Z_{380K} ..	58
Figure 18. Global distribution of mean CIN in OPFs at different reference levels. (a) Z_{LRT} , (b) Z_{CP} , and (c) Z_{380K} ..	57
Figure 19. Geographical distribution of highest MLS water vapor values (ppmv) at 100 hPa. The MLS water vapor values categorized by the different numbers are shown in symbols of different colors.	58
Figure 20. Cases for high MLS water vapor value and their meteorology environmental in different regions. (a) US, (b) Argentina. The time and levels for different dataset are shown in the title.	59

LIST OF TABLES

TABLES	PAGE
Table 1. Population of Overshooting Precipitation Features (OPFs) identified with different reference heights*	36
Table 2. Occurrence of 15 dBZ and 20 dBZ at Different Reference Heights	39
Table 3. Global Distribution of OPFs Overshooting Area Using Different Reference Heights (units %).....	40

1. Introduction

The troposphere is relatively isolated from the stratosphere, because the troposphere is characterized by low static stability with strong vertical exchange through convection and circulations, in contrast to prevalent slow vertical air motion in the stratosphere. However, the dynamics of troposphere and stratosphere are inseparable [e.g., Hoskins et al., 1985]. Air mass brought into the stratosphere from the troposphere in the tropics is part of the larger scale Brewer-Dobson circulation [Randel et al., 2006]. The circulation is characterized by rising tropical motion followed by poleward transport and descending motion in the extratropical stratospheres. Stratosphere-troposphere exchange has an important impact on atmosphere dynamic, chemistry and radiation. On the other hand, it is important to correctly describe the process of stratosphere-troposphere exchange in the climate models to be able to fully understand global climate change [Holton et al., 1995]. Vertical transport of air and chemical species from the troposphere into the stratosphere via deep convection plays an important role in the process of stratosphere-troposphere exchange. Fueglistaler et al. [2004] revealed that tropical convection penetrating the tropopause may lead to fast transport of air from the troposphere into the stratosphere. This fast transport process provides an important control on stratospheric composition, which may also alter the radiative balance in the Tropical Tropopause Layer (TTL) [Yang et al., 2010]. There is also evidence that convection may penetrate into the stratosphere [Fischer et al., 2003; Liu and Zipser, 2005] and have an important impact on the amount of water vapor there [Homeyer et al., 2014]. A 1% increase of stratospheric water vapor per year has been

reported over the past 50 years [Oltmans and Hofmann, 1995; Rosenlof and Kley, 2001]. However, the reason for the observed increase is still not clear at the present [Sherwood et al., 2010]. The variations of stratospheric water vapor, a possible contributor to observed stratospheric cooling [Shindell, 2001], may have also played an important role in the stratospheric radiative balance [Forster and Shine, 1999] and ozone depletion [Kirk-Davidoff et al., 1999]. As a result, understanding the processes controlling the stratospheric water vapor content is vitally important.

Although it has long been known that air entering the stratosphere through the tropical tropopause is freeze dried [Brewer, 1949], the roles of different physical processes transporting the water vapor from the troposphere into the stratosphere are still under debate [Sherwood and Dessler 2000; Jensen et al. 1996; Schoeble et al. 2014]. In addition to the large scale upwelling [Randel and Jensen, 2013] and horizontal transport [Holton and Gettelman, 2001], deep convection has been identified as potentially important in the dehydration process of air entering the stratosphere [Alcala and Dessler, 2002; Danielsen, 1982; Sherwood and Dessler,2002].

To understand the role of deep convection in the vertical transport of trace gases in the stratosphere, it is necessary to quantify the distribution of convection reaching the tropopause. To further provide a global illustration of this distribution, Gettelman et al. [2002] have searched the cloud regions colder than the tropopause temperatures on infrared images and identified numerous extremely cold clouds over the Western Pacific region. The launch of Tropical

Rainfall Measuring Mission (TRMM) in November 1997, covering the Earth from 35°S to 35°N, improved our knowledge of the vertical structure of deep convection in the tropics [Kummerow et al., 2000]. Acala and Dessler [2002] and Liu and Zipser [2005] presented the properties of deep convection and their distribution over the tropics with the precipitation radar onboard the TRMM. These studies focus on the convection over the tropics, where the Brewer-Dobson circulation initiates [Plumb and Eluszkiewicz, 1999; Boehm and Lee, 2003].

Previous works also showed that convective storms in the mid-latitude may also penetrate into the lowermost stratosphere [Poulida et al., 1996; Fischer et al., 2003; Dessler, 2009; Homier et al., 2014], and even into the “overworld” (defined as that part of the stratosphere at which potential temperature (θ) surfaces are always above the tropopause (i.e., $\theta > 380$ K; Holton 1995; Fromm and Seryranckx, 2003; Jost et al., 2004; Livesey, 2004; Ray et al., 2004]). Recently, Anderson et al. [2012] have argued that deep convection at mid and high-latitudes could be an effective pathway to inject water vapor into the stratosphere and has a significant impact on the ozone concentrations. Therefore, it is important to quantify the frequency of these storms and their relative importance to those in the tropics.

Some cases of the mid-latitude storms have been studied with numerical models in the past [e.g. Park and Droegemeier, 2000; Mullendore, 2005]. These case studies suggest that convection at mid-latitudes is a complicated process and many factors may affect a storm’s properties and evolution. Clouds from mid-latitude storms have also been studied with global satellite

observations such as geostationary infrared images [Bedka et al., 2010; Setvak et al., 2007] and CloudSat cloud radar reflectivities [Mace et al., 2009; Stevens and Feingold, 2009; Yang et al., 2010]. However, infrared images do not provide the details of storms under cold cloud shields. CloudSat observations are only available at near 0130 and 1330 local times, and miss the important convection in the late afternoon over land [Augustine, 1984; Nesbitt and Zipser, 2003; Liu et al. 2008].

As the successor of TRMM, the Global Precipitation Measurement (GPM) core satellite was launched in February 2014. This international collaborative satellite mission provides next-generation observations of rain and snow worldwide at a high temporal resolution [Hou et al., 2014]. The core satellite has both radar and passive microwave radiometers that may quantify the properties of cloud systems and their distributions with a global coverage from 65°S to 65°N. Especially, the radar reflectivity observations may directly indicate the vertical structure and intensity of deep convection. Figure 1 shows an example of deep convection penetrating the tropopause over central North America (42°N). In this case, the tropopause is derived using the lapse rate definition (WMO, 1957) and is found at 13.3 km. The detectable radar reflectivity reaches 16 km. The area with 20 dBZ radar reflectivity or higher at the tropopause is approximately 2750 km². Observations from the GPM core satellite provide a unique opportunity to study the properties of cloud systems like the case shown in Figure 1. Using the GPM radar observations collected during the first year, this study aims to identify the convection reaching the tropopause and quantify their distributions globally. The main scientific questions include:

- In the tropics, does the GPM show a distribution of deep convection reaching the tropopause similar to what the TRMM has demonstrated in the past?
- How frequent do deep convective storms penetrate into the stratosphere at the mid and high latitudes? What are the characteristics of these storms compared to those in the tropics?
- What is the global geographical distribution of convection reaching the tropopause and their relative frequencies? How do they vary seasonally and diurnally?

To address these questions, first we identify the convective storms reaching the tropopause by combining the GPM radar observations and meteorological environments. Then we present their geographical distribution, occurrence frequency, seasonal and diurnal variations. We also explore the depth of these storms at different reference levels in the tropics, subtropics, and mid and high latitudes. The data and methodology are presented in section 2, the results are shown in section 3, and the summary and discussion are included in section 4.

2. Data and method

The core observatory of GPM carries the first spaceborne Dual-frequency Precipitation Radar (DPR), which is operating at Ku and Ka bands [Hou et al., 2014]. The 65° inclination orbit allows it to sample global precipitation systems over more than 90% of the globe with a variety

of instruments. Since its launch in February 2014, the GPM core satellite has collected millions of snapshots of global precipitation systems [Liu and Zipser, 2015]. In this study we use a similar approach as Liu and Zipser [2005] to identify the storms reaching the tropopause. We then apply this to mid and high latitudes with the GPM observations. First, the Precipitation Features (PFs) are defined by grouping the contiguous areas with non-zero near surface precipitation derived using GPM Ku band radar [Seto et al. 2013]. Within each PF, the maximum heights with detectable Ku radar reflectivity, 15 dBZ and 20 dBZ, are summarized as proxies of the tops of the storms. The numbers of pixels with Ku radar reflectivity greater than 15 and 20 dBZ are counted at altitudes from 1 to 19 km with 0.5 km intervals in each PF. Large-scale meteorological conditions at the time and the location of each PF, including profiles of temperature, geopotential height, relative humidity, and parameters at surface, are obtained from the ERA-Interim reanalysis dataset [Dee et al. 2011] after spatial and temporal interpolation. The latest version of the ERA-Interim dataset with 0.75° horizontal resolution, 6 hourly intervals at 37 pressure levels is used here.

Quantifying the tropopause reaching storms globally needs to be done with care because there exist multiple tropopause definitions [e.g., Holton 1995; Pan et al. 2004; Kunz et al. 2011; Munchak and Pan 2014]. The choices of critical levels are often made based on the specific scientific questions. In order to fully characterize the extent of deep convection, six different reference levels are considered in this analysis. In the tropics (20° S- 20° N), we consider 14 km level ($Z_{14\text{km}}$) and the Level of Neutral Buoyancy (Z_{LNB}). The 14 km level has been used to

approximate the lower boundary of the TTL [Alcala and Dessler, 2002; Liu and Zipser 2005; Fueglistaler et al. 2009]. Z_{LNB} has been used to estimate the cloud tops based on the parcel model assuming moist adiabatic process in an undiluted convective core. The Z_{14km} and Z_{LNB} are used here mainly for comparisons to the TRMM statistics over the tropics in Liu and Zipser [2005]. At the mid-high latitudes (30° - 65° N/S), we use heights of two PVU surface (Z_{PV}), where PVU presents the standard Potential Vorticity Unit ($1 \text{ PVU} = 10^{-6} \text{ K m}^2 \text{ kg}^{-1} \text{ s}^{-1}$) [Holton et al., 1995]. Potential Vorticity (PV), as an air-mass tracer, has been used to separate stratospheric and tropospheric air sources [Hoskins et al. 1985; Raymond 1992; McIntyre and Norton 2000; Kunz et al. 2011]. Globally, we consider the lapse rate tropopause (Z_{LRT} , WMO, 1957), level of 380 K potential temperature surface (Z_{380K}), and the height of the Coldest Point (Z_{CP}) in the temperature profile. The WMO definition Z_{LRT} can be applied globally [Randel et al. 2006, Munchak and Pan 2014]. Z_{380K} has been used as the boundary between the lowermost stratosphere and the “overworld” [Holton et al. 1995; Appenzeller et al. 1996; Stohl et al. 2003]. The coldest point in the temperature profile has been recognized as the key factor controlling the “freeze and dry” process [Ueyama et al., 2014; Holton and Gettelman, 2001; Gettelman et al. 2002] and is used to define the Cold-Point Tropopause in the tropics. Note that in the tropics, Z_{LRT} and Z_{CP} are very close to each other. Because of the unique role of Z_{CP} in dehydration, we computed the Z_{CP} and Z_{LRT} separately and presented both despite the possible redundancy.

To calculate these reference levels for each PF, first, ERA-Interim temperature, geopotential height, and PVU profiles are interpolated into the time and location of each PF. Then, such

profiles are further spline interpolated into 0.1 km vertical intervals. Then, Z_{LNB} , Z_{380K} , Z_{LRT} , Z_{PV} and Z_{CP} are calculated with the interpolated vertical profiles. Though these reference levels have precision of 0.1 km, the real vertical resolution of the ERA-Interim temperature and PVU profiles is much coarse. Considering temporal, spatial, and vertical interpolations, as well as the uncertainties in ERA-Interim product itself, these reference levels could have large uncertainties. However, we will show that the general conclusions are the same when different reference levels are used.

To quantify the global distribution of convective systems reaching high altitudes, the Overshooting PFs (OPFs) are defined as the PFs with the maximum heights of the GPM Ku band radar echo tops at 15 dBZ, and 20 dBZ above the reference levels respectively. The areas of 15 dBZ and 20 dBZ at different reference levels are also calculated within each OPF. Because the current early-released version of GPM products still has some noises in its radar reflectivity profiles, quality control of the data is necessary. In this study, we insist that OPFs with echo tops above the reference levels require at least 4 contiguous pixels with surface precipitation (i.e., OPF size is greater than $\sim 100 \text{ km}^2$); OPFs with echo tops above 17 km must have significant ice scattering signals from passive microwave radiances (GPM GMI minimum 89 GHz brightness temperature less than 220 K), and the difference between the maximum 15 and 20 dBZ echo tops is less than 5 km in order to ensure a physically reasonable radar reflectivity vertical profile at the convective core. The vertical profiles of the areas of 15 and 20 dBZ within PFs are also examined to remove the PFs with no detectable echoes at levels below the maximum echo top

heights. Following these procedures, the illegitimate OPFs due to the artifacts in the radar products are significantly reduced.

Figure 2a-2e shows the two-dimensional histograms of reference levels Z_{LNB} , Z_{380K} , Z_{LRT} , Z_{CP} , and Z_{PV} at different latitudes for all PFs. Different reference levels are binned into 5° latitude zones with 0.5 km vertical intervals. With typical values between 12-16 km in the tropics, Z_{LNB} has an asymmetrical distribution between the northern and the southern tropics and a larger variation in southern tropics (Figure 2a). At high latitudes, most of the precipitation systems are baroclinic and are driven by temperature and pressure gradients. Z_{LNB} is no longer a meaningful predictor for cloud tops, except in the case of some barotropic systems during the summer. Therefore, we only use Z_{LNB} as the reference level of the storm over 20°S - 20°N . Z_{380K} has values around 16-18 km in the tropics. At the mid and high latitudes, Z_{380K} varies between 12 and 15 km, and is nearly symmetric between the Northern and Southern Hemisphere (Figure 2b). Most Z_{LRT} are about 16-18 km and are close to the Z_{380K} in the tropics (Figure 2c). Z_{LRT} at high latitudes is about 8-12 km, with a nearly symmetric latitudinal structure between the Northern and Southern Hemispheres. Consistent with previous studies [Munchak and Pan, 2014], Z_{CP} is close to Z_{LRT} in the tropics but much higher and larger variations in the mid-high latitudes (Figure 2d). Because of the unique role of Z_{CP} in dehydration associated with the vertical motion and the larger uncertainty in the data, we computed the Z_{CP} and Z_{LRT} separately and presented both despite the small difference between them in mid-high latitudes. The high Z_{CP} values at

mid-high latitudes mainly occur during the cold season (Figure didn't show this here). Later, we will show that Z_{CP} values at the mid and high latitudes are usually lower than 13 km when Overshooting occur in summer season. Z_{PV} as the dynamical tropopause is only used over the extratropics (excluding 30°S-30°N) [Holton et al., 1995]. The dynamical tropopause is relatively more uniform in the Northern Hemisphere than in the Southern Hemisphere. More Z_{PV} concentrate in 6-8 km in Southern Hemisphere. Comparing with the tropopause, Z_{PV} has a broader range in the mid-latitudes (30°-40°).

To demonstrate PFs with radar echo tops above these references heights, Figure 2f shows a two-dimensional histogram of the maximum 20 dBZ echo top heights in the PFs. The mean reference levels at different latitudes from Figure 2a-2e are shown as individual curves in Figure 2f. In the tropics, the mean heights of Z_{LRT} , Z_{CP} and Z_{380K} are close to each other and are about 1-2 km higher than the mean Z_{LNB} . At mid-high latitudes, the mean Z_{LRT} is about 4 km lower than Z_{380K} and 1 km higher than Z_{PV} , which is consistent with Kunz et al. [2004]. Most PFs do not have 20 dBZ echo tops reaching Z_{LNB} due to weak updrafts with significant entrainments in convection. A small fraction of PFs do reach above the mean of tropopause in the tropics, and are consistent with previous research [Gettelman et al. 2002; Liu and Zipser 2005; Yang et al. 2010]. Some of them may even reach above 19 km in the tropics [Zipser et al. 2006]. At the mid and high latitudes, the values of 20 dBZ echo top heights have asymmetrical distributions with higher echo tops and larger variations in the Northern Hemisphere than in the Southern Hemisphere. At the mid-high latitudes south of 40°S, most of the PFs have 20 dBZ echo top

below 5 km. Almost all of them are below the mean heights of Z_{LRT} , Z_{PV} and Z_{380K} . This is consistent with previous works stating that the clouds over the Southern Ocean are mostly below 5 km [Haynes et al., 2011; Williams et al., 2013]. However, PFs have large variations of radar echo tops at the northern mid-high latitudes. Though the majority of mid-high latitude PFs have 20 dBZ echo tops below 6 km, some of them may reach above 10 km, higher than the mean Z_{LRT} , Z_{PV} , and Z_{380K} . Though mean Z_{CP} at mid-high latitudes seems to be above all the PFs echo tops in Figure 2f, we will show that Z_{CP} are usually below 13 km when OPFs occur during boreal summer time..

In addition to the uncertainties of reference levels, we also have to be careful on the determination of the tropopause and echo tops. For example, the true tropopause and coldest point might be influenced by deep convection at the local scale that is not resolved by the reanalysis data. On the other hand, since the horizontal resolution of GPM Ku radar is about 5 km, smaller scale overshooting could be overestimated by radar beam filling. The detectable signal of 15 and 20 dBZ echo tops are used as the storm tops in this study. They may be inferred as thick cloud tops with large size ice particles. However, the true storm cloud tops could be higher.

3. Results

After grouping contiguous precipitating areas using the GPM Ku radar retrievals, more than two

million PFs with at least 4 pixels are identified from March 2014 to February 2015 in the 65°S-65°N latitudes [Liu and Zipser, 2015]. OPFs are identified with the maximum heights of detectable radar echoes at 12 dBZ (MAXHT), 15 dBZ (MAXHT15) and 20 dBZ (MAXHT20) greater or equal to the different reference levels. The total numbers of OPFs corresponding to different reference levels are listed in Table 1. Lesser OPFs are identified when a higher reference level is used. Only 1630 OPFs are found with echo tops above Z_{380K} . More OPFs are identified with minimum detectable echoes at 12 dBZ than those with 15 dBZ and 20 dBZ echo tops. It is common that lower radar reflectivity reaches higher altitudes near the tops of convective cores. The radar reflectivity is observed as decreasing with height near convection tops because a smaller amount of ice particles with smaller sizes are lifted up to higher altitudes, and radar reflectivity is sensitive to both size and total number of ice particles. It is expected that the real cloud tops will be above the height of the minimum detectable signal (~12 dBZ) by the Ku radar [Hamada and Takayabu, 2015]. Therefore, it is probable that more OPFs would be detected if radar with a higher sensitivity were used.

3.1 Geographical distribution of OPFs

Figure 3 shows the locations of OPFs defined with a height of 20 dBZ reaching above different reference levels. The geographical distributions of OPFs vary when different reference levels are used. OPFs reaching above 14 km are situated mainly in the tropics and subtropics (dots in Figure 3a). They are found over Central Africa, Amazon, the Inter Tropical Convergence Zone

(ITCZ), and the South Pacific Convergence Zone (SPCZ), which shows a good correspondence with the results from the TRMM [Liu and Zipser, 2005]. At the mid-high latitudes north of 40°N and south of 40°S, OPFs above 14 km are only found over central North America.

In the tropics, OPFs greater than Z_{LNB} are found over Central Africa, Amazon, the ITCZ, and the SPCZ, consistent with the results from the TRMM [Liu and Zipser, 2005]. Tall OPFs with echo tops 3 km higher above Z_{LNB} (blue, orange and red dots in Figure 3b) are mainly found over land regions, including Amazon and Central Africa.

Consistent with Liu and Zipser [2005], the majority of OPFs reaching above the Z_{LRT} and Z_{380K} are over land in the tropics and subtropics, such as the Central Africa, Amazon, Argentina, and Panama (Figure 3c, 3d and 3f). At the mid and high latitudes, OPFs above Z_{LRT} and Z_{CP} are found over central North America, Europe, and Northern Russia. There are less storms reaching above Z_{CP} than Z_{LRT} (Figure 3c and 3d). Though most of the PFs are below the mean coldest point in mid-high latitude (Figure 2f), there are still individual PFs, mainly in the summer season (June, July August), reaching above the coldest point over central North America, Europe and Russia. When referring to the dynamical tropopause (Z_{PV}), many OPFs are found over central North America, Europe and Russia. Many OPFs above Z_{PV} are found over the ocean in mid and high latitudes, especially in the southern oceans. There are fewer OPFs with 20 dBZ echo tops greater than Z_{380K} , especially at high latitudes over Europe and Northern Russia (Figure 3f). OPFs above Z_{380K} are mainly found over the Central Africa, South America, and the SPCZ.

Comparing Figure 3c, Figure 3d and Figure 3e, most OPFs penetrating the tropopause over Russia and Europe do not reach Z_{380K} . Note that it is very rare to see a PF with radar echoes reaching above Z_{LRT} and Z_{CP} and Z_{380K} over the southern oceans.

Most of the PFs are below the mean coldest point height at mid-high latitudes (Figure 2f), however, the Z_{CP} -reaching OPFs are found with higher frequency over central North America, Europe and Russia in Northern Hemisphere (Figure 3e). To clarify this, histograms of different reference levels when OPFs occur in different latitude zones are shown in Figure 4. In northern high latitudes, Z_{380K} is about 14-16 km and is the highest among all the reference levels (Figure 4a). Z_{CP} is about 12 km and close to Z_{LRT} in northern high latitude. Though most of Z_{CP} values are higher than 14 km in Figure 2d, most of the OPFs occur in summer time when Z_{CP} is lower and close to Z_{LRT} . The close values of Z_{CP} and Z_{LRT} over northern mid-high latitude in summer are also reported by Munchak and Pan [2014]. Z_{PV} has a large variation from 4 km to 13 km. In the northern subtropics and mid latitudes (Figure 4b), when the OPFs occur, Z_{380K} is about 2 km higher than in the high latitudes. Most Z_{CP} are above 14 km in the subtropics. Z_{LRT} have values ranging from 7 km to 18 km. Z_{PV} could extend up to 16 km in the northern subtropics. In the tropics (Figure 4c), Z_{LRT} , Z_{CP} and Z_{380K} are close around 17 km. Z_{LNB} is about 1-2 km lower than other reference levels. In southern subtropics (Figure 4d), Z_{PV} is about 1-2 km lower in South Hemisphere than in Northern Hemisphere. In the southern high latitude (Figure 4e), OPFs above Z_{380K} and Z_{CP} are rare and their reference level histograms are not shown. Z_{PV} and Z_{LRT} are slightly lower than in the northern high latitudes. In general, Figure 4 demonstrates that there is a

large variation of reference levels at different latitudes when OPFs occur.

Figure 5 further shows that the reference levels such as Z_{CP} vary significantly when OPFs occur over different regions in the same latitudinal zone. At northern high latitudes (Figure 5a), OPFs reaching Z_{CP} are found over several longitudinal regions in Figure 3d. The OPFs above Z_{CP} over 60°W - 120°W , mainly from the central North America, could reach 18 km. the OPF above Z_{CP} from Europe and Russia (0 - 125°E) are about 12-14 km. The relatively “shallow” OPFs happen over North Atlantic Ocean (-20°W - 0°W). In the northern subtropics, the OPFs reaching the coldest point are found over North America and Asian monsoon (Figure 5b). The most noteworthy feature in northern subtropics is the “taller” OPFs from the Asian monsoon. In the tropics (Figure 5c), all of the OPFs, mainly from Amazon, Central Africa and SPCZ (Figure 3d), are above 14 km, some even reaching 20 km. In the southern subtropics (Figure 5d), the OPFs over Argentina are about 17-19 km, while the OPFs over Australia have two corresponding heights. In Southern Australia, the OPFs heights are usually below 14 km and occur mainly in the spring and fall seasons. In the northern region of Australia, the OPFs heights are above 17 km, and occur mainly in the winter season.

We have shown the locations of OPFs and their overshooting distance above the reference levels. However, OPFs could have different impacts on vertical transport due to their sizes, especially the size of their convective cores at the reference levels. To address this, the areas of 15 dBZ and 20 dBZ at various references levels are calculated for each OPF. Their mean areas in $5^{\circ}\times 5^{\circ}$ grids

are shown in Figure 6. In general, the OPFs have a larger mean area at different reference levels in mid and high latitudes than they do in the tropics. The regions, including central North America, Argentina, Europe and Central Africa, have the largest mean areas of 20 dBZ at the reference levels.

After dividing the total area of 15 and 20 dBZ at reference levels with the total sampled area, the occurrences of OPFs areas in five different latitude zones are summarized in Table 2. In the tropics, occurrences of 15 and 20 dBZ at 14 km in tropics are about 40 times higher than in the subtropics. However, occurrences of 15 and 20 dBZ at Z_{LRT} are about 60-70% higher in northern high latitudes than they are in the tropics. Compared to the tropopause, occurrences of 15 and 20 dBZ at Z_{CP} are relatively smaller (about 15-40% higher in northern high latitudes than that in the tropics). Occurrences of 15 and 20 dBZ at Z_{PV} at high latitudes are about twice as high as those at Z_{LRT} . It is not surprising that the occurrence frequencies of 15 and 20 dBZ above Z_{380K} are the lowest because Z_{380K} is the highest among all the reference levels. Only 0.0007% of the total sample area is found with 20 dBZ radar reflectivity at the tropopause in the tropics. This is one order smaller than the 0.008% as reported in Liu and Zipser [2005]. This difference may be due to different datasets. In Liu and Zipser [2005], the tropopause values were from the NCEP tropopause product. Here the tropopause is calculated with the latest ERA-interim reanalysis dataset. ERA-Interim reanalysis dataset has a 0.75° horizontal resolution while the NCEP tropopause has a 2.5° horizontal resolution. It is also possible that there are still some calibration differences between the TRMM and the GPM. Nevertheless, the difference in the occurrences

from this study in regards to Liu and Zipser [2005] indicates that large uncertainties exist in the estimates of OPF occurrences at the tropopause. These uncertainties could be due to large uncertainties in the definition of reference levels and limited sample sizes.

Figure 7 presents the geographical distribution of occurrences of 20 dBZ in OPFs at different reference levels. The occurrences are calculated by dividing the number of pixels with 20 dBZ at each reference level by the total sample pixels of Ku radar in each $5^{\circ} \times 5^{\circ}$ box. Consistent with Liu and Zipser [2005], three hotspots with high occurrences of 20 dBZ at 14 km are found over Central Africa, Panama, and Argentina (Figure 7a). Compared to the numerous OPFs over the ITCZ Ocean and Amazon (Figure 3a), the OPFs over these three regions have larger mean 20dBZ area at 14 km lead to higher occurrences there. Figure 7b shows the geographical distribution of the occurrences of 20 dBZ at Z_{LRT} . Consistent with Figure 3c, in addition to the hotspots over the tropical land, 20 dBZ is also frequently found at tropopause levels over northern high latitude lands, such as Russia and Europe. Note that hotspot of high occurrence of 20 dBZ at Z_{LRT} stands out over central North America. The geographical distribution is similar when using the coldest point (Figure 7c). Using a higher reference level only changes the magnitude of the occurrence of the OPFs but not the spatial pattern (Figure 7b and Figure 7c). In addition to over land at mid and high latitudes, OPFs above the dynamic tropopause (Z_{PV}) are also frequently found over ocean at mid and high latitudes (Figure 7d). The hotspots over central North America and Argentina also stand out at Z_{380K} (Figure 7e). This means that the OPFs over central North America and Argentina, such as the one shown in Figure 1, have significant

contribution of 20 dBZ area at Z_{LRT} , Z_{CP} and Z_{380K} compared to those over the tropics. In general, though PFs reaching above 14 km are frequently found over oceans (Figure 7a), PFs over land are more likely to reach the tropopause, the coldest point and Z_{380K} . OPFs that reach Z_{PV} in mid-high latitudes are more frequent when compared to Z_{CP} , Z_{LRT} and Z_{380K} , especially over ocean. The regions with high occurrences of convection reaching above the tropopause include Panama, Argentina, Central Africa, and central North America (Figure 3b, Figure 3c and 3d).

To show the regional difference of OPFs, the fractional contribution of OPFs area at references in eight longitudinal regions over the tropics ($20-20^\circ$) subtropics ($20-40^\circ$) and high latitude ($40-65^\circ$) as shown in Figure 7e are calculated and listed in Table 3. In the tropics, the contributions from Africa ($0-45^\circ E$) and South America ($90-45^\circ W$) dominate among the eight regions. This is consistent with previous results [Liu and Zipser, 2005]. In the northern subtropics, North America ($135-90^\circ W$ and $90-45^\circ W$) and Asian monsoon ($90-135^\circ E$) play the most important role in the area contribution. In northern high latitudes, the contribution is mostly from North America and Russia. The OPFs area at Z_{380K} from North America alone is more than 80%. In the southern subtropics, more than 50% of the OPF overshooting area is from Argentina ($90-45^\circ W$).

3.2 Seasonal variation of zonal mean distribution of OPFs

In order to show the seasonal variations of OPFs, the zonal distributions of population, mean 20

dBZ areas at the tropopause per OPF, and occurrences of 20 dBZ at the tropopause during different seasons are shown in Figure 8. In general, two regions are found with larger numbers of OPFs reaching the tropopause: the tropics between 20°S and 15°N and the mid-high latitudes in the Northern Hemisphere (30°N-60°N) (Figure 8a). In the tropics, the locations of OPFs migrate with the ITCZ during different seasons. In the subtropics and mid-high latitudes, more OPFs are found in summer than in winter. At mid-high northern latitudes, OPFs are dominant in June, July, and August (JJA) mainly over central North America (Figure 8a). Figure 8b shows that OPFs reaching the tropopause have relatively smaller 20 dBZ areas at the tropopause in the tropics than those at the mid-high latitudes. The peak in JJA at 40°N is contributed mainly by OPFs over central North America, including Nebraska, Iowa, and Minnesota. Though numerous OPFs are found in the tropics (Figure 8a), the OPFs at mid-high latitudes have larger overshooting areas per storm (Figure 6 and Figure 8b), and may play an important role in the cross-tropopause transport. This is clearly confirmed in Figure 8c. The 20 dBZ areas at the tropopause over 40°N-45°N are even slightly larger than in the tropics in the first year of the GPM observation (black curve in Figure 8c). In JJA (red curve in Figure 8c), the peak of fractional occurrence of 20 dBZ at the tropopause is about 4 times higher at northern mid-high latitudes than the peak in the tropics. The zonal occurrences of 20 dBZ areas at the tropopause vary significantly in different seasons. This can be due to the variation of both OPF population and size in the tropopause.

Figure 9 shows the zonal distributions of populations, mean 20 dBZ areas at the coldest point per

OPF, and occurrences of 20 dBZ at the coldest point during different seasons. In general, the patterns remain similar compared to Figure 8. However, the peak for the coldest point in mid-high latitudes is relatively lower. To show the role of OPFs to the “overworld” above 380 K [Holton et al. 1995], the zonal distributions of population, mean area and occurrences of 20 dBZ of OPFs at Z_{380K} are shown in Figure 10. Consistent with Figure 3 and 6, frequent deep convection penetrating Z_{380K} is mainly found in the tropics (Figure 10a). There are fewer storms reaching Z_{380K} at the high latitudes. Though relatively rare, the mean 20 dBZ area of OPFs at Z_{380K} is larger in mid-high latitudes at 30° and 40° (Figure 7d and Figure 10b), especially those over Argentina and central North America. These OPFs are the main reason for the high 20 dBZ occurrence at Z_{380K} over the subtropics and mid latitudes, especially in summer (Figure 10c).

Though there is a clear peak of high 20 dBZ occurrences at mid-high latitudes shown in Figure 8c, Figure 9c and Figure 10c, we still need to take into account that the total surface area of the 5° latitude band is smaller at high latitudes than in the tropics. Therefore, to evaluate the global budget of the overshooting area from convective storms in whole, after applying the factor of cosine (latitude) to Figure 8c, the fractional contribution of annual 20 dBZ areas at Z_{LRT} from different latitudes and seasons is shown in Figure 11a. The areas with 20 dBZ at the tropopause are dominantly from both the tropics and northern mid-high latitudes. In JJA, OPFs in the mid-high latitudes in the Northern Hemisphere (40°N - 60°N) have a contribution greater than those in the tropics. These OPFs are located mainly over central North America. Compared with the tropopause, OPFs above the coldest point in the mid-high latitude have a slightly smaller

contribution than those in the tropics (Figure 11b). However, the OPFs at mid-high latitudes only have relatively weaker impacts on the “overworld” indicated by smaller contributions of 20 dBZ above Z_{380K} at high latitudes (Figure 11c). Differently from Figure 11a, the major peak in the tropics is significantly greater than at 40°-45° N in Figure 11c. Comparing the mid-high latitudes between the Northern and Southern Hemispheres, the contributions from OPFs at Z_{380K} over 10°-30° S in DJF appear larger than those over central North America in JJA (Figure 11c).

To utilize the higher precision and greater sensitivity that the GPM Ku radar has compared to TRMM [Hou et al., 2014; Seto et al. 2014], a similar analysis with areas of 15 dBZ is shown in Figure 11d, Figure 11e and 11f. The fractional contribution of annual overshooting 15 dBZ areas at Z_{LRT} , Z_{CP} and Z_{380K} from different latitudes and seasons shows a similar two-peak distribution to the distribution when using 20 dBZ. The contribution of overshooting 15 dBZ areas at the tropopause from mid-high latitudes is still greater than that in tropics (Figure 11d). However, the proportions of contributions from the tropics and mid-high latitudes are different at the coldest point using 20 dBZ. When the 15 dBZ is used, the areas at the coldest point in the tropics are larger than they are at the mid and high latitudes (Figure 11e). This implies that the storms with relatively weaker radar echoes reaching the coldest point are more populated in the tropics than they are in the mid-high latitudes.

3.3 Diurnal Variation of OPFs

Figure 12a shows the diurnal variation of OPF populations in the tropics. Consistent with

previous works [Liu and Zipser, 2005], the diurnal variation of convection over continents is stronger than it is over oceans. The peak of OPF population over land is in the afternoon. The diurnal variation of oceanic systems is weak, as it has been noted by previous literature [e.g. Hendon and Woodberry, 1993; Chen and Houze, 1997; Nesbitt and Zipser, 2003]. The diurnal variation of OPFs over subtropical land is similar to the variation in the tropics (Figure 12b). The diurnal variations of OPFs over the subtropics and mid-high latitude oceans are not shown due to the limited samples. At mid-high latitudes, the diurnal variations of OPFs reaching Z_{380K} is noisy because of the smaller sample size (Figure 12c), but still shows the afternoon peak. It is worth noting that the peak in mid-high latitude OPFs reaching tropopause (Z_{LRT} and Z_{CP}) over land is broader than that in tropics and subtropics in the afternoon. We speculate that in summer, the sun rises earlier at high latitudes and a longer period of morning sensible heating leads to an earlier peak of instability. Therefore, deep convection would peak slightly broader. This broader peak diurnal structure warrants further investigation. Since the diurnal variation at high latitudes is not the focus of this study, the topic is not discussed further.

3.4 Vertical structure of OPFs

To investigate the characteristic of the OPFs, the mean maximum reflectivity of OPFs above the different levels over different regions are shown in Figure 13. In general, maximum radar reflectivity decreases with height. Maximum radar reflectivity at high altitudes is larger over land than over ocean (Figure 13a). The OPFs in the mid-high latitude land are mainly from Russia

and Europe, which makes the profile in Russia coincide with the profile over land in the mid-high latitudes. The profile in the US is close to the profile in the subtropics land. The maximum radar reflectivity at the mid-levels (7-10 km) over land in the subtropics approximates to that in the tropics. The maximum radar reflectivity at the mid-levels (7-14 km) is larger when Z_{CP} (Figure 13b) and Z_{380K} (Figure 13c) are used as reference levels. The profile over ocean in the mid-high latitudes is not shown because there are no OPFs penetrating Z_{380K} over ocean (Figure 13c). The maximum radar reflectivity of OPFs above Z_{380K} is always larger compared to those above Z_{LRT} and Z_{CP} .

Figure 14 shows the vertical mean area of 20 dBZ of OPFs in the different regions. Similar to the maximum radar reflectivity, the mean area of 20 dBZ decreases with altitude. The area of 20 dBZ at low levels (< 9 km) is larger over ocean than over land. However, the OPFs are close to each other at mid-levels (9-12 km) (Figure 14a and 14b). The OPFs above Z_{380K} are larger compared to Z_{LRT} and Z_{CP} (Figure 14c). The area of OPFs penetrating Z_{380K} in different regions at the mid-high levels (>9 km) is approximated to each other.

To investigate the prevalence of large ice particles in the convection, the mean area of 30 and 40 dBZ of OPFs in different regions are shown in Figures 15 and 16. The radar reflectivity of 30 dBZ OPFs above Z_{LRT} could reach above 14 km over land in the tropics and subtropics, even over tropic oceans (Figure 15a). Compared to other regions, the radar reflectivity of 30 dBZ of OPFs penetrating the tropopause over ocean in the mid-high latitudes is lower. The modest peak

at about 5 km indicates the freezing level. The radar reflectivity of 30 dBZ could be higher than 14 km over the subtropics ocean when Z_{CP} reference levels are used. Z_{380K} -OPFs is the strongest among all the OPFs. That is why the radar reflectivity of 30 dBZ in all regions could be above 14 km (Figure 15c).

The radar reflectivity of 40 dBZ indicates large hail size ice particles, so the maximum heights of 40 dBZ reach lower than those of 20 and 30 dBZ. The OPFs are stronger over land in the subtropics than those in the tropics. When Z_{380K} is used, the radar reflectivity of 40 dBZ the OPFs over land in the subtropics and mid-high latitudes, including US and Europe, are larger than those in the tropics. Note that the US has the distinction of experiencing stronger convection than other regions.

3.5 Large scale environments of OPFs

Deep convection is regarded as developing spontaneously within a large-scale environment in which the vertical profiles of temperature and moisture play an important role. Convection feeds on the convective available potential energy (CAPE). Figure 17 shows the geographical distribution of the mean CAPE of OPFs above different reference levels. The mean CAPE of OPFs is larger in the tropics than in the extratropics, especially over Panama, Argentina, Central Africa, and the SPCZ. The mean CAPE in the US, Europe and Russia is relatively lower compared with the mean CAPE in the tropics. On the other hand, in order to support vigorous

deep convection, air parcels need to reach their level of free convection to release high CAPE. Hence, the convective inhibition energy (CIN) at the top of the planetary boundary layer also plays a role in setting the stage for building up the CAPE for convective storms. The mean CIN of OPFs is shown in Figure 18. The large mean CIN coincides with the high occurrence of OPFs in US, Europe, Russia, Argentina, and Central Africa (Figure 7). Large CIN values make it difficult for the air parcels to reaching the level of free convection. However, once the buoyant air parcels is lifted up to the level of free convection by some large-scale forcing mechanism such as extratropical cyclones, or more localized forcing mechanism, such as a sea-breeze front, a range of hill, the convection could be very vigorous and tall. To further understand the behavior of overshooting convection, other factors, such as extreme convection to the synoptic-scale, the complex topography, and the diurnal cycle of heating need to be studied in the future work.

3.6 Linkage between high water vapor values in the low stratosphere and deep convection

As shown in this study, in addition to high occurrence of overshooting deep convection in the tropics, we also found that convections penetrating the tropopause at northern mid-high latitudes are as frequent as those over the tropics, especially in summer. Some of the mid-high latitude deep convection could even reach the “overworld”, especially in central North America and Argentina. However, these results still cannot answer whether the tropopause-reaching convective storms would play a major role in the vertical transport of water vapor into the stratosphere. To demonstrate this, the extreme high water vapor values at 100 hPa from the

10-year observations of AURA Microwave Limb Sounder (MLS) are shown in Figure 19. The high water vapor values (red and blue dots) are found over the ITCZ, Asian Monsoon, and the US, while the extreme water vapor values (black dots) are found in Argentina, the US, and Asian Monsoon. It is easy to speculate that the high water vapor concentrations are related to deep convection penetrating the tropopause. To prove this, two cases of high MLS, water vapor value, and the ambient environment adopted from ERA-Interim reanalysis dataset are shown in Figure 20. The extreme water vapor values are observed near or above the deep clouds in the US and Argentina. Combining the wind field from the ERA-Interim, the content of the water vapor is very likely from the vertical transport of deep convection that could reach near the tropopause. Further investigation on this is warranted with more observations and evidence.

3. 7 Uncertainties and implications to the convective vertical transports

Though we have demonstrated the locations of overshooting storms and the areas of 15 and 20 dBZ radar echoes at the multiple references levels of interest to various transport analyses, there is still a gap between the areas of storms at tropopause and the estimation of the amount of trace gas vertically transported into the stratosphere through convection, especially for water vapor.

Firstly, 15 and 20 dBZ radar echoes at the tropopause only represent the precipitation hydrometeors at high levels. The clouds with small ice particles are not detected. Some weak convective clouds (more prevalent in the tropics) reaching the tropopause are not included in these analyses. Secondly, radar echoes above the tropopause only demonstrate that large ice

particles are injected into the stratosphere. However, it is very likely that only a small portion of these ice particles would stay and sublimate. Overshooting tops are negatively buoyanted and tend to quickly fall back to the troposphere. Though there is evidence that some ice particles would be left behind [e.g. Corti et al. 2005], the detrainment rate of ice particles from overshooting tops and the details of this process are still unknown. Thirdly, there is still a large uncertainty in the estimation of the overshooting convection from satellite observations due to the uncertainty of tropopause height. A slight difference in the reference levels could lead to significant variations in the overshooting area. It is clear that different tropopause definitions may lead to significant differences in the overshooting area occurrence estimates (Table 2 and Table 1 in Liu and Zipser [2005]). Lastly, only one-year of GPM observations are used in this study. The overshooting storms are rare events. Some of the quantitative results in this study would possibly require more observations to validate them in the future. Nevertheless, here we have applied several different reference levels in the overshooting definitions, and they all confirm several geographical hotspots of the overshooting storms. The geographical distributions of the overshooting storms and their relative contributions should be qualitatively valid.

4. Summary

With the dual frequency radar onboard and a 65° inclination orbit, the GPM core satellite provides a unique opportunity to investigate the properties of deep convection with a global perspective. In this study, the deep convective storms with tops near the tropopause are identified

with different reference levels using one-year GPM Ku band radar observations. In the tropics, the distribution of deep convection reaching near the tropopause agrees well with the results demonstrated by Liu and Zipser [2005] with the TRMM dataset, e.g. high occurrence of overshooting deep convection over land, especially over Panama and Central Africa.

One of the most important findings of this study is the relative importance of overshooting storms over mid-high latitude land in the Northern Hemisphere. Our analysis shows that overshooting storms at mid-high latitudes (mainly from central North America) in the Northern Hemisphere have comparable areas of radar echo at the tropopause with those in the tropics in this one-year data. In boreal summer months, the total tropopause reaching OPFs area is even greater in the Northern Hemisphere mid-high latitudes than that in the tropics. The tropopause reaching convection over central North America and Argentina have larger areas at the tropopause than those in tropics. They may have an important contribution to trace gas transport from the troposphere to the stratosphere. However, we also find that these tropopause-penetrating storms at the mid and high latitudes only occasionally reach 380 K potential temperature level and are less frequent than those in the tropics.

Since most of the overshooting storms are over land, they have strong seasonal and diurnal variations. Seasonally, the locations of overshooting storms are associated with the migrations of the ITCZ and monsoons. Diurnally, most of the overshooting storms occur in the mid-late afternoon.

The OPFs above Z_{CP} and Z_{380K} in the subtropics are stronger than those in the tropics, with higher radar reflectivity at high altitudes. The overshooting storms with large CIN in the subtropics land are found over the US and Argentina, while those in the mid-high latitudes land are found mainly over Europe and Russia. The tropopause-reaching convection have a potential to transport water vapor into the lower stratosphere. Such candidate cases are shown in the US and Argentina.

Though one-year GPM observations have shown a global distribution of deep convective storms with updrafts of sufficient strength to penetrate the tropopause and even into the “overworld”, it is still difficult to quantify the vertical transport of trace gases into the stratosphere associated with these storms. The definition of tropopause heights and the unknown detrainment processes at these altitudes still remain challenges in understanding the mechanism of overshooting convection in the troposphere and stratosphere exchanges.

Reference:

Alcala, C. M., and Dessler, A. E. (2002). Observations of deep convection in the tropics using the Tropical Rainfall Measuring Mission (TRMM) precipitation radar. *J. Geophys. Res. Atmos.*, **107(24)**. doi:10.1029/2002JD002457

- Anderson, J. G., Wilmouth, D. M., Smith, J. B., and Sayres, D. S. (2012). UV dosage levels in summer: increased risk of ozone loss from convectively injected water vapor. *Science*, **337(6096)**, 835-839.
- Appenzeller, C., J. R. Holton, and K. H. Rosenlof (1996), Seasonal variation of mass transport across the tropopause, *J. Geophys. Res.*, **101(D10)**, 15071–15078, doi:10.1029/96JD00821.
- Augustine, J. A. (1984). The Diurnal Variation of Large-Scale Inferred Rainfall over the Tropical Pacific Ocean during August 1979. *Mon. Weather Rev.* doi:10.1175/1520-0493.
- Bedka, K., (2011) Overshooting cloud-top detections using MSG SEVIRI infrared brightness temperatures and their relationship to severe weather over Europe. *Atmos. Res.*, **99**, 175–189.
- Boehm, M. T., and Sukyoung Lee, (2003). The Implications of Tropical Rossby Waves for Tropical Tropopause Cirrus Formation and for the Equatorial Upwelling of the Brewer–Dobson Circulation. *J. Atmos. Sci.*, **60**, 247–261. doi: <http://dx.doi.org/10.1175/1520-0469>
- Brewer, A. W. (1949). Evidence for a World Circulation Provided By the Measurements of Helium and Water Vapour Distribution in the Stratosphere. *Q. J. R. Meteorol. Soc.*, **75**, 351–363. doi:10.1002/qj.49707532603.
- Chen, S. S., and Houze Jr, R. A. (1997). Diurnal Variation and Life-Cycle of Deep Convective Systems over the Tropical Pacific Warm Pool. *Q. J. R. Meteorol. Soc.* doi:10.1002/qj.49712353806.
- Corti, T., Luo, B. P., Peter, T., Vömel, H., and Fu, Q. (2005). Mean radiative energy balance and vertical mass fluxes in the equatorial upper troposphere and lower stratosphere. *Geophys. Res. Lett.*, **32**, L06802, doi:10.1029/2004GL021889.
- Danielsen, E. F. (1982), A dehydration mechanism for the stratosphere. *Geophys. Res. Lett.*, **9**: 605–608. doi:10.1029/GL009i006p00605
- Dee, D. P., Uppala, S. M., Simmons, A. J., Berrisford, P., Poli, P., Kobayashi, S., ... Vitart, F. (2011). The ERA-Interim reanalysis: Configuration and performance of the data assimilation system. *Q. J. R. Meteorol. Soc.*, **137(656)**, 553–597. doi:10.1002/qj.828
- Dessler, A. E., and S. C. Sherwood (2004), Effect of convection on the summertime extratropical lower stratosphere, *J. Geophys. Res.*, **109**, D23301, doi:10.1029/2004JD005209.
- Fischer, H., et al. (2003), Deep convective injection of boundary layer air into the lowermost stratosphere at midlatitudes, *Atmos Chem Phys*, **3**, 739 – 745.

- Forster, P. M. D. F., and Shine, K. P. (1999). Stratospheric water vapour changes as a possible contributor to observed stratospheric cooling. *Geophys. Res. Lett.*, **26(21)**, 3309–3312. doi:10.1029/1999GL010487
- Fromm, M. D. (2003). Transport of forest fire smoke above the tropopause by supercell convection. *Geophys. Res. Lett.*, **30(10)**, 10–13. doi:10.1029/2002GL016820
- Fueglistaler, S. (2004). Tropical troposphere-to-stratosphere transport inferred from trajectory calculations. *J. Geophys. Res.*, **109(D3)**, 1–16. doi:10.1029/2003JD004069
- Fueglistaler, S., A. E. Dessler, T. J. Dunkerton, I. Folkins, Q. Fu, and P. W. Mote (2009), Tropical tropopause layer, *Rev. Geophys.*, **47**, RG1004, doi:10.1029/2008RG000267.
- Gettelman, A. (2002). Distribution and influence of convection in the tropical tropopause region. *J. Geophys. Res.*, **107(D10)**. doi:10.1029/2001JD001048
- Hall, T. J., and Vonder Haar, T. H. (1999). The Diurnal Cycle of West Pacific Deep Convection and Its Relation to the Spatial and Temporal Variation of Tropical MCSs. *J. Atmos. Sci.*, **56(19)**, 3401–3415. doi:10.1175/1520-0469
- Hamada, A., and Y. N. Takayabu, (2015). Improvements in Detection of Light Precipitation with the Global Precipitation Measurement Dual-Frequency Precipitation Radar (GPM/DPR), *J. Atmos. Ocean. Tech.*, doi:10.1175/JTECH-D-15-0097.1
- Haynes, J. M., Jakob, C., Rossow, W. B., Tselioudis, G., and Brown, J. B. (2011). Major characteristics of Southern Ocean cloud regimes and their effects on the energy budget. *J. Clim.*, **24(19)**, 5061–5080. doi:10.1175/2011JCLI4052.1
- Hendon, H. H., and K. Woodberry (1993), The diurnal cycle of tropical convection, *J. Geophys Res.* **98(D9)**, 16623–16637, doi:10.1029/93JD00525.
- Holton, J. R., and Gettelman, A. (2001). Horizontal transport and the dehydration of the stratosphere. *Geophys. Res. Lett.*, **28(14)**, 2799–2802. doi:10.1029/2001GL013148
- Holton, J. R., Haynes, P. H., McIntyre, M. E., Douglass, A. R., Rood, R. B., and Pfister, L. (1995). Stratosphere-troposphere exchange. *Rev. Geophys.*, **33(4)**, 403. doi:10.1029/95RG02097
- Homeyer, et al. (2014), Convective transport of water vapor into the lower stratosphere observed during double tropopause events, *J. Geophys. Res. Atmos.* **119**, 10,941–10,958, doi: 10.1002/2014JD021485.

- Hoskins, B. J., M. E. McIntyre, and A. W. Robertson, On the use and significance of isentropic potential vorticity maps, *Q. J. R. Meteorol. Soc.*, 111,877-946, 1985.
- Hou, A. Y., Kakar, R. K., Neeck, S., Azarbarzin, A. A., Kummerow, C. D., Kojima, M., ... Iguchi, T. (2014). The global precipitation measurement mission. *Bull. Am. Meteorol. Soc.*, **95(5)**, 701–722. doi:10.1175/BAMS-D-13-00164.1
- Jensen, E. J., Toon, O. B., Pfister, L., and Selkirk, H. B. (1996). Dehydration of the upper troposphere and lower by subvisible cirrus clouds near the tropical tropopause, *Geophys. Res. Lett.* , **23(8)**, 825–828.
- Jost, H. J., Drdla, K., Stohl, A., Pfister, L., Loewenstein, M., Lopez, J. P., ... Xueref, I. (2004). In-situ observations of mid-latitude forest fire plumes deep in the stratosphere. *Geophys. Res. Lett.*, **31(11)**, 1–5. doi:10.1029/2003GL019253
- Kirk-Davidoff, D. B., Hints, E. J., Anderson, J. G., and Keith, D. W. (1999). The Effect of Climate Change on Ozone Depletion through Changes in Stratospheric Water Vapour., *Nature*, **402** 399-401, doi:10.1038/46521
- Kummerow, C., Simpson, J., Thiele, O., Barnes, W., Chang, A. T. C., Stocker, E., ... Nakamura, K. (2000). The Status of the Tropical Rainfall Measuring Mission (TRMM) after Two Years in Orbit. *J. Appl. Meteorol.*, **39(12)**, 1965–1982. doi:10.1175/1520-0450(2001)040<1965:TSOTTR>2.0.CO;2.
- Kunz, A., P. Konopka, R. Müller, and L. L. Pan (2011), Dynamical tropopause based on isentropic potential vorticity gradients, *J. Geophys. Res.*, **116**, D01110, doi:10.1029/2010JD014343.
- Liu, C., and E. J. Zipser (2005). Global distribution of convection penetrating the tropical tropopause. *J. Geophys. Res. Atmos.*, **110(23)**, 1–12. doi:10.1029/2005JD006063.
- Liu, C., Zipser, E. J., Mace, G. G., and Benson, S. (2008a). Implications of the differences between daytime and nighttime CloudSat observations over the tropics. *J. Geophys. Res. Atmos.*, **114(8)**, 1–11. doi:10.1029/2008JD009783
- Liu, C., and E. J. Zipser (2015), The global distribution of largest, deepest, and most intense precipitation systems. *Geophys. Res. Lett.*, **42**, 3591–3595. doi: 10.1002/2015GL063776.
- Livesey, N. J. (2004). CN observed by the Upper Atmosphere Research Satellite Microwave Limb Sounder following boreal forest fires. *J. Geophys. Res.*, **109(D6)**, 1–9. doi:10.1029/2003JD004055

- Mace, G. G., Zhang, Q., Vaughan, M., Marchand, R., Stephens, G., Trepte, C., and Winker, D. (2009). A description of hydrometeor layer occurrence statistics derived from the first year of merged Cloudsat and CALIPSO data. *J. Geophys. Res. Atmos.*, **114**(8), 1–17. doi:10.1029/2007JD009755.
- McIntyre, M., (1988). The dynamical significance of isentropic distributions of potential vorticity and low-level distributions of potential temperature. *Proc. The Nature and Prediction of Extratropical Weather Systems*, Vol. 1, Reading, United Kingdom, ECMWF, 237–259.
- Mullendore, G. L., Durran, D. R., and Holton, J. R. (2005). Cross-tropopause tracer transport in midlatitude convection. *J. Geophys. Res. D Atmos.*, **110**(6), 1–14. doi:10.1029/2004JD005059.
- Munchak, L. A. and L. L. Pan (2014), Separation of the lapse rate and the coldpoint tropopauses in the tropics and the resulting impact on cloud top – tropopause relationships, *J. Geophys. Res. Atmos.* **119**, 7963-7978, doi:10.1002/2013JD021189.
- Nesbitt, S. W., and Zipser, E. J. (2000). A census of precipitation features in the tropics using TRMM: Radar, ice scattering, and lightning observations. *J. Clim.*, **13**(23), 4087–4106. doi:10.1175/1520-0442
- Nesbitt, S. W., and Zipser, E. J. (2003). The diurnal cycle of rainfall and convective intensity according to three years of TRMM measurements. *J. Clim.*, **16**(10), 1456–1475. doi:10.1175/1520-0442-16.10.1456.
- Oltmans, S.J., and D.J. Hofmann (1995), Increase in lower-stratospheric water vapor at a midlatitude N.H. site from 1981 to 1994, *Nature*, **374**, 146-149.
- Pan, L. L., W. J. Randel, B. L. Gary, M. J. Mahoney, and E. J. Hints (2004), Definitions and sharpness of the extratropical tropopause: A trace gas perspective, *J. Geophys. Res.*, **109**, D23103, doi:10.1029/2004JD004982.
- Park, S. K., and Droegemeier, K. K. (2000). Sensitivity Analysis of a 3D Convective Storm: Implications for Variational Data Assimilation and Forecast Error. *Mon. Weather Rev.*, **128**(1), 140–159. doi:10.1175/1520-0493(2000)128<0140:SAOACS>2.0.CO;2
- Plumb, R. A., and Eluszkiewicz, J. (1999). The Brewer-Dobson circulation: Dynamics of the tropical upwelling. *J. Atmos. Sci.*, **56**(6), 868-890.

- Poulida, O., R. R. Dickerson, and A. Heymsfield, Stratosphere-troposphere exchange in a midlatitude mesoscale convective complex, 1, Observations, *J. Geophys. Res. Atmos.*, **101**, 6823-6836, 1996.
- Randel, W. J., F. Wu, H. Vömel, G. E. Nedoluha, and P. Forster (2006), Decreases in stratospheric water vapor after 2001: Links to changes in the tropical tropopause and the Brewer-Dobson circulation, *J. Geophys. Res.*, **111**, D12312, doi:10.1029/2005JD006744.
- Randel, W. J., Seidel, D. J., and Pan, L. L. (2007). Observational characteristics of double tropopauses. *J. Geophys. Res. Atmos.*, **112**(7), 1–13. doi:10.1029/2006JD007904.
- Randel, W. J., and Jensen, E. J. (2013). Physical processes in the tropical tropopause layer and their roles in a changing climate. *Nat. Geosci.*, **6**(3), 169–176. doi:10.1038/ngeo1733.
- Ray, E. A., Rosenlof, K. H., Richard, E. C., Hudson, P. K., Cziczo, D. J., Loewenstein, M., ... Herman, R. L. (2004). Evidence of the effect of summertime midlatitude convection on the subtropical lower stratosphere from CRYSTAL-FACE tracer measurements. *J. Geophys. Res. Atmos.*, **109**(18), 1–13. doi:10.1029/2004JD004655.
- Raymond, D. J., 1992: Nonlinear balance and potential-vorticity thinking at large Rossby number. *Quart. J. Roy. Meteor. Soc.*, 118, 987–1015.
- Rosenlof, H., and Kley, D. (2001). Stratospheric water vapor over the past half-century, *Geophys. Res. Lett.*, **28**(7), 1195–1198.
- Schoeberl M. R., A. E. Dessler, T. Wang, M. A. Avery, and E. J. Jensen (2014), Cloud formation, convection, and stratospheric dehydration, *Earth and Space Science*, **1**, 1–17, doi:10.1002/2014EA000014.
- Schwartz, M. J., Read, W. G., Santee, M. L., Livesey, N. J., Froidevaux, L., Lambert, A., and Manney, G. L. (2013). Convectively injected water vapor in the North American summer lowermost stratosphere. *Geophys. Res. Lett.*, **40**(10), 2316-2321.
- Seto, S., Iguchi, T., and Oki, T. (2013). The basic performance of a precipitation retrieval algorithm for the global precipitation measurement mission's single/dual-frequency radar measurements. *IEEE Trans. Geosci. Remote Sens.*, **51**(12), 5239–5251. doi:10.1109/TGRS.2012.2231686.
- Setvák, M., Rabin, R. M., and Wang, P. K. (2007). Contribution of the MODIS instrument to observations of deep convective storms and stratospheric moisture detection in GOES and MSG imagery. *Atmos. Res.* **83**(2), 505-518.

- Sherwood, S. C., and A. E. Dessler (2000). On the control of stratospheric humidity. *Geophys. Res. Lett.*, **27**, 2513 – 2516.
- Sherwood, S. C., R. Roca, T. M. Weckwerth, and N. G. Andronova (2010), Tropospheric water vapor, convection, and climate, *Rev. Geophys.*, **48**, RG2001, doi: 10.1029/2009RG000301
- Shindell, D. T. (2001), Climate and ozone response to increased stratospheric water vapor, *Geophys. Res. Lett.*, **28**(8), 1551–1554, doi:10.1029/1999GL011197.
- Solomon, S., Rosenlof, K. H., Portmann, R. W., Daniel, J. S., Davis, S. M., Sanford, T. J., and Plattner, G.-K. (2010). Contributions of stratospheric water vapor to decadal changes in the rate of global warming. *Science*, **327**(5970), 1219–1223. doi:10.1126/science.1182488.
- Steven C. Shrewood Andrew E. Dressler. (2000). On the control of stratospheric humidity. *Geophys. Res. Lett.*, **73**(5), 275–276. doi: 10.1029/2000GL011438.
- Stevens, B., and Feingold, G. (2009). Untangling aerosol effects on clouds and precipitation in a buffered system. *Nature*, **461**(7264), 607–613. doi:10.1038/nature08281.
- Stohl, A., et al. (2003), Stratosphere-troposphere exchange: A review, and what we have learned from STACCATO, *J. Geophys. Res.*, **108**, 8516, doi:10.1029/2002JD002490, D12.
- Ueyama, R., E. J. Jensen, L. Pfister, G. S. Diskin, T. P. Bui, and J. M. Dean-Day (2014), Dehydration in the tropical tropopause layer: A case study for model evaluation using aircraft observations, *J. Geophys. Res. Atmos.*, **119**, 5299–5316, doi:10.1002/2013JD021381.
- Williams, K. D., Bodas-Salcedo, A., Déqué, M., Fermepin, S., Medeiros, B., Watanabe, M., ... Williamson, D. L. (2013). The transpose-AMIP II experiment and its application to the understanding of southern ocean cloud biases in climate models. *J. Clim.*, **26**(10), 3258–3274. doi:10.1175/JCLI-D-12-00429.1
- World Meteorological Organization (WMO), (1957), *Meteorology A Three-Dimensional Science: Second Session of the Commission for Aerology*, WMO Bulletin IV(4), WMO, Geneva, 134 – 138.
- Yang, Q., Fu, Q., and Hu, Y. (2010). Radiative impacts of clouds in the tropical tropopause layer. *J. Geophys. Res. Atmos.*, **115**(4), 1–21. doi:10.1029/2009JD012393.

Appendix

Table 1. Population of Overshooting Precipitation Features (OPFs) identified with different reference heights*

	Maxht (#)	15 dBZ (#)	20 dBZ (#)
>14 km	15090	12779	9890
> Z_{LNB}^*	9415	8388	3145
> Z_{LRT}	4537	3709	2648
> Z_{PV}^*	4320	4040	3267
> Z_{CP}	2484	1848	1473
> Z_{380K}	1636	1163	878

* Z_{PV} is applied over extratropics (30°S-65°S and 30°N-65°N); Z_{LNB}^* is applied over 20°S -20°N

TABLES

Table 2. Occurrence of 15 dBZ and 20 dBZ at Different Reference Heights

Reference height	60°S-40°S	40°S -20°S	20°S -20°N	20°N -40°N	40°N -60°N	
15 dBZ	14 km	2.0e-08	2.7e-05	2.2e-04	5.0e-05	4.8e-06
	Z _{LRT}	3.5e-06	1.2e-05	1.4e-05	1.6e-05	2.2e-05
	Z _{CP}	3.1e-07	2.5e-06	8.7e-06	4.0e-06	1.0e-05
	Z _{PV}	2.2e-05	7.7e-05*		1.0e-04*	5.4e-05
	Z _{380K}	5.3e-09	3.0e-06	8.7e-06	3.7e-06	1.8e-06
20 dBZ	14 km	0.0	1.5e-05	9.5e-05	2.5e-05	3.0e-06
	Z _{LRT}	9.4e-07	5.3e-06	6.5e-06	7.3e-06	1.1e-05
	Z _{CP}	1.2e-07	1.3e-06	4.0e-06	2.2e-06	5.5e-06
	Z _{PV}	4.5e-06	2.4e-05*		3.8e-05*	2.3e-05
	Z _{380K}	0.0	1.7e-06	4.3e-06	1.9e-06	1.2e-06

* is calculated over 30°-40°

Table 3. Global Distribution of OPFs Overshooting Area Using Different Reference Heights (units %)

%		Reference Heights	180-135°W	135-90°W	90-45°W	45-0°W	0-45°E	45-90°E	90-135°E	135-180°E
40°N- 65°N	Z _{LRT}	0.2	32.8	2.5	4.4	24.7	12.7	20.8	1.9	
	Z _{CP}	0.2	34.2	2.2	1.4	19.6	15.8	24.3	2.4	
	Z _{PV}	0.8	20.5	2.7	10.0	27.7	12.9	21.8	3.4	
	Z _{380K}	0	83.9	2.6	0	11.4	0.2	0.9	1.0	
20°N- 40°N	14 km	0.7	25.7	19.1	0.2	0.8	21.0	26.8	5.7	
	Z _{LRT}	3.0	26.5	26.8	5.7	17.1	12.3	5.1	3.5	
	Z _{CP}	0	34.6	42.5	0.6	2.0	6.8	7.9	5.5	
	Z _{PV}	8.0*	16.4*	17.2*	9.5*	17.9*	11.5*	7.3*	12.2*	
	Z _{380K}	0.1	32.9	20.9	0	0	20.5	20.8	4.7	
20°S- 20°N	14 km	3.6	4.6	19.0	5.8	26.4	7.3	19.3	14.0	
	Z _{LNB}	2.8	3.7	31.7	8.5	27.7	7.7	9.2	8.8	
	Z _{LRT}	2.1	4.2	23.1	6.8	29.3	5.3	18.2	10.9	
	Z _{CP}	2.2	3.7	20.0	6.3	29.4	5.9	20.3	12.3	
	Z _{380K}	1.5	2.9	19.2	5.8	30.5	7.5	21.1	11.6	
20°S- 40°S	14 km	3.7	0.4	65.9	2.2	11.3	3.8	3.3	9.3	
	Z _{LRT}	3.8	4.0	57.2	7.2	6.9	2.0	2.8	16.1	
	Z _{CP}	2.3	0.8	77.0	0.8	0.4	2.2	0.2	16.2	
	Z _{PV}	14.1*	3.7*	17.5*	3.7*	22.0*	4.8*	4.4*	29.8*	
	Z _{380K}	0.6	0	82.6	1.9	3.0	2.2	0	9.6	

40°S-	Z _{LRT}	12.4	12.1	15.5	3.5	3.2	4.3	17.7	31.2
	Z _{CP}	1.6	0	0	6.5	6.8	0	0	85.1
65°S	Z _{PV}	12.8	12.5	23.9	4.0	5.3	6.5	11.6	23.4
	Z _{380K}	0	0	0	0	0	0	0	0

* is calculated over 30°-40°

FIGURES

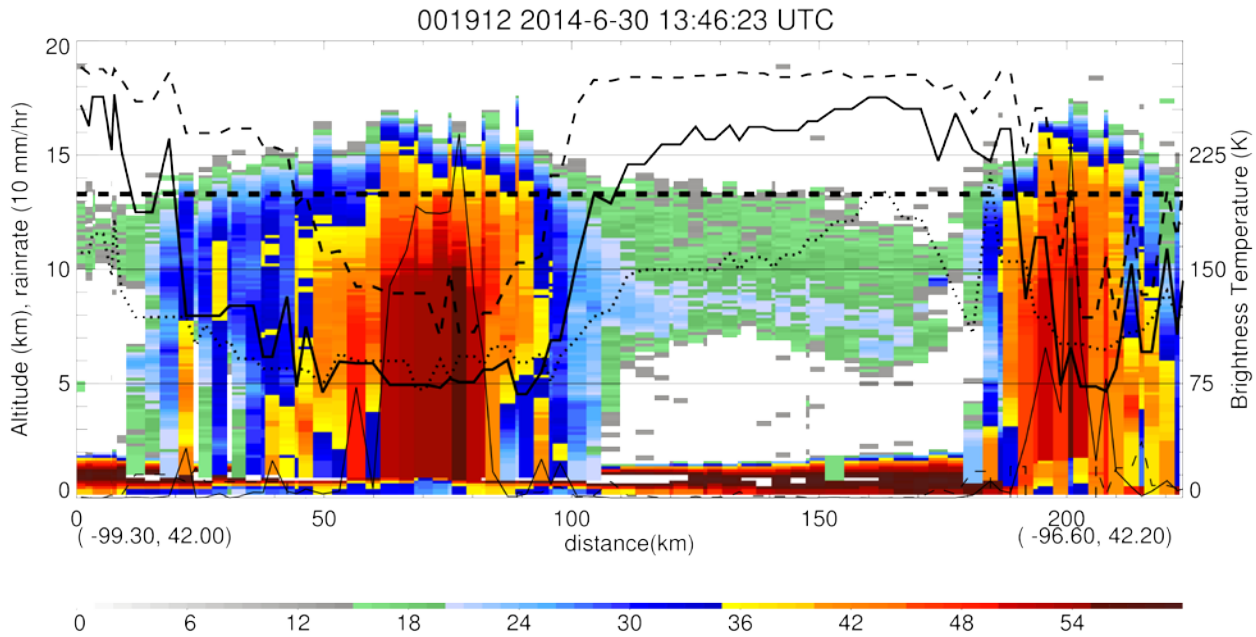


Figure 1. An example of deep convection reaching above tropopause over Nebraska, United States. Color fill is the Ku radar reflectivity. The dotted, dashed and solid lines are GPM Microwave Imager (GMI) brightness temperatures at 183 ± 7 , 37 and 89 GHz. The lapse rate tropopause height derived from ERA-Interim is 13.3 km. The area with 20 dBZ at 13.3 km in this storm is 2750 km².

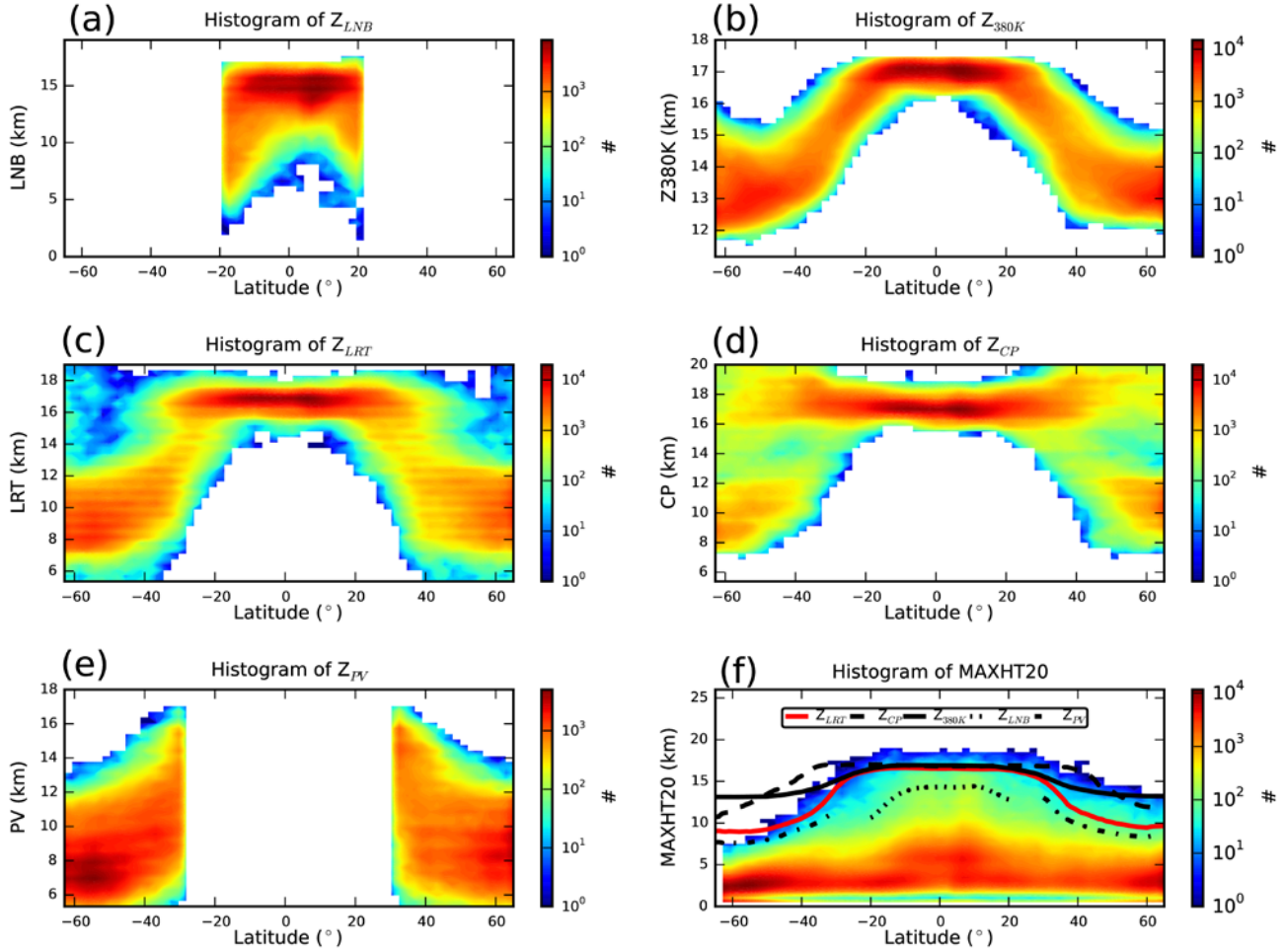


Figure 2. Two dimensional histogram of various reference levels at different latitudes derived from ERA-Interim reanalysis for PFs. (a) Level of Neutral Buoyancy (Z_{LNB}). (b) Height with potential temperature at 380 K (Z_{380K}), (c) Lapse Rate Tropopause (Z_{LRT}). (d) The Coldest Point (Z_{CP}). (e) Height with Potential Vorticity Unit at 2 (Z_{PV}). (f) Two dimensional histogram of maximal 20 dBZ echo top heights in PFs. The mean Z_{LRT} , Z_{CP} , Z_{380K} , Z_{PV} and Z_{LNB} are overlaid.

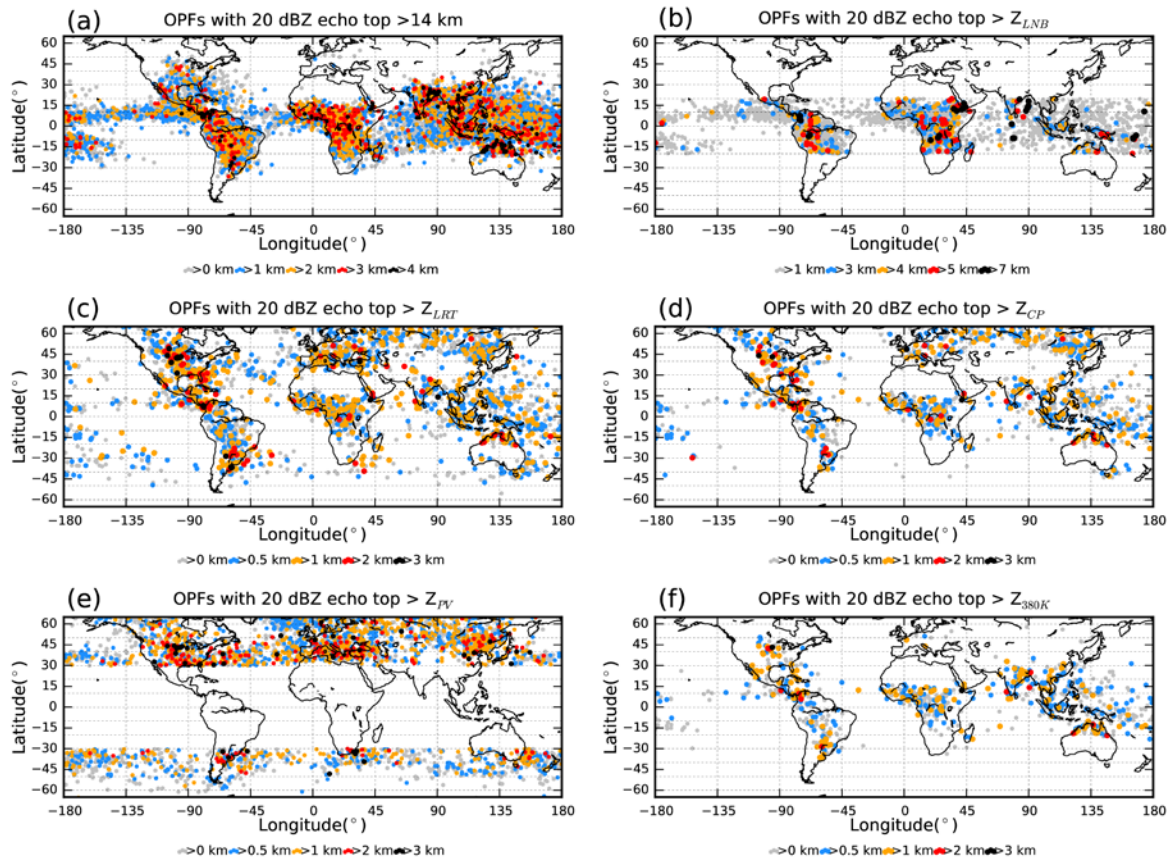


Figure 3. Locations of OPFs identified with different reference levels. (a) 14 km, (b) Z_{LNB} , (c) Z_{LRT} , (d) Z_{CP} , (e) Z_{PV} , and (f) Z_{380K} . The PFs categorized by the overshooting distance above the reference levels are shown in symbols of different colors.

Histogram of reference heights of OPFs

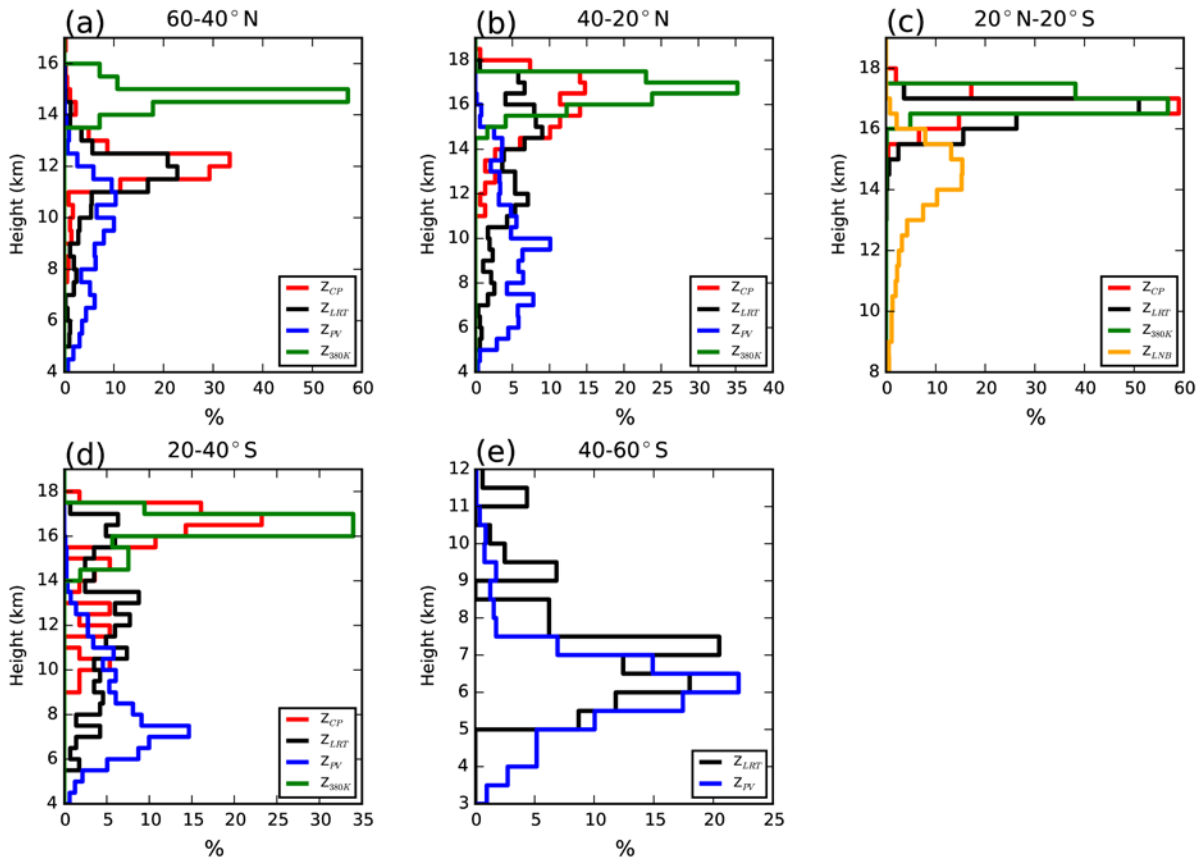


Figure 4. Histogram of various reference levels when OPFs occur in different latitude zones. (a) 40°N-60°N. (b) 20°N-40°N. (c) 20°S-20°N. (d) 20°S-40°S. (e) 40°S-60°S.

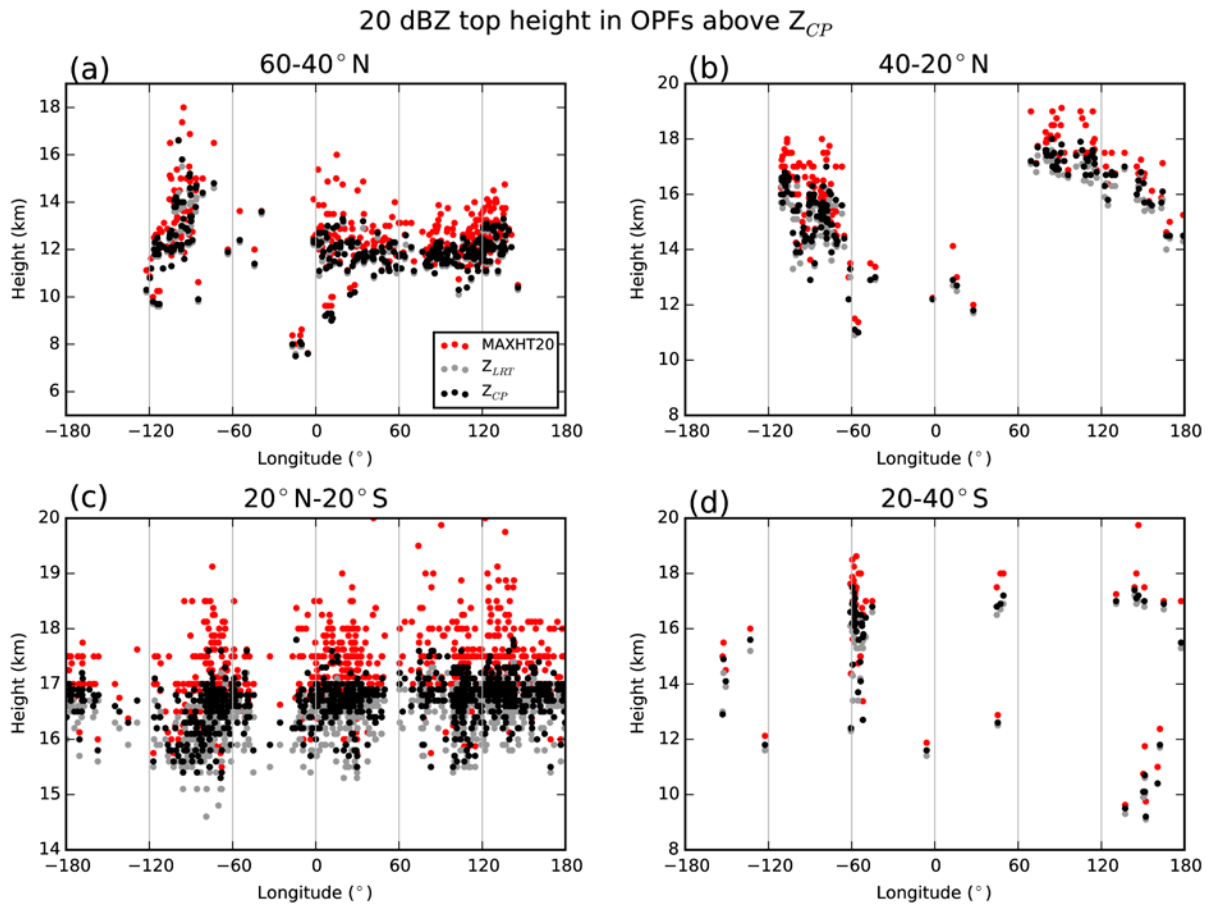


Figure 5. Maximum 20 dBZ echo top heights (red dots) of OPFs reaching above Z_{CP} . The reference levels Z_{CP} are shown with black dots. Z_{LRT} are shown with gray dots. (a) 40°N - 60°N . (b) 20°N - 40°N . (c) 20°S - 20°N . (d) 20°S - 40°S .

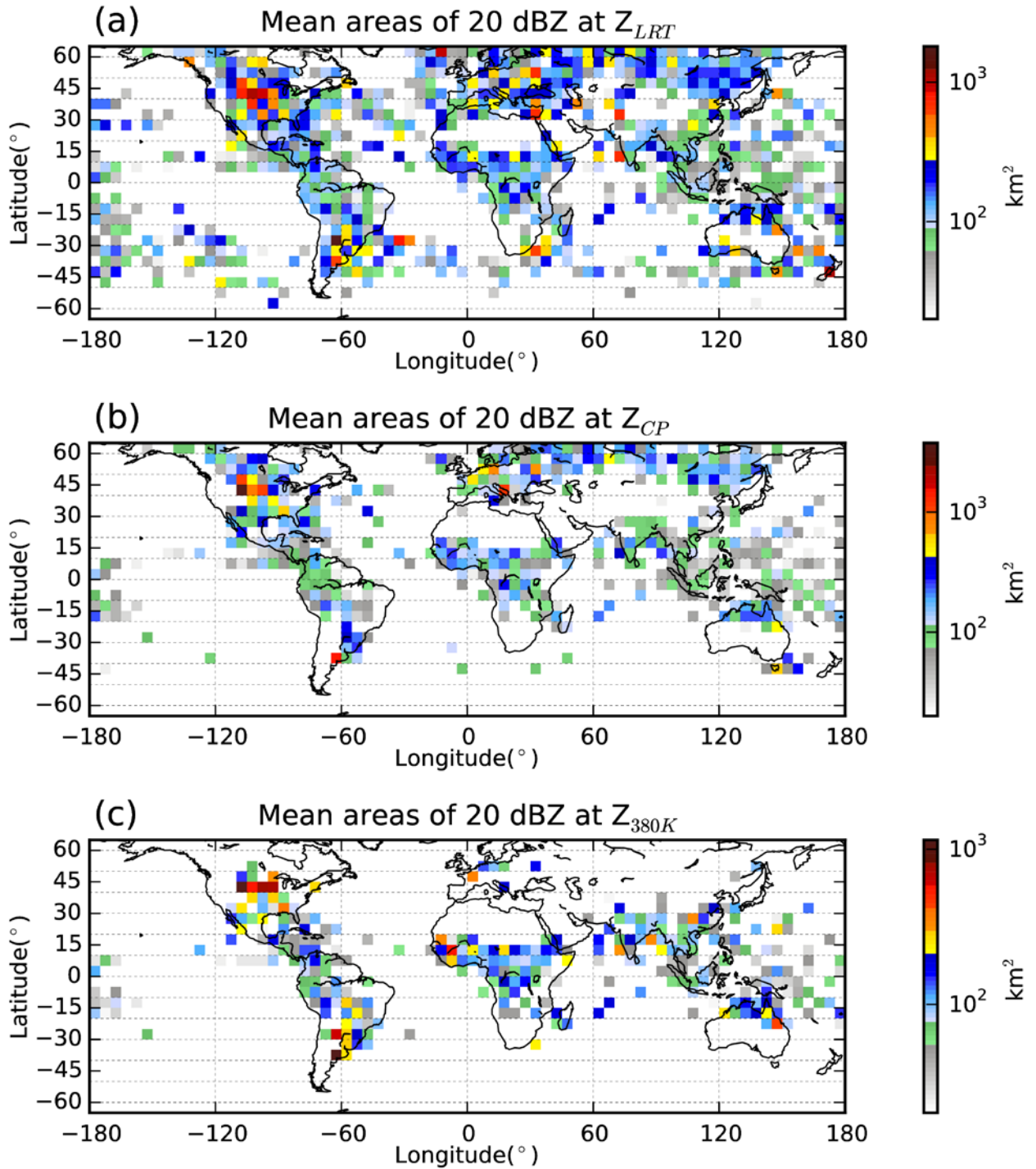


Figure 6. Global distribution of area of 20 dBZ in OPFs at different reference levels. (a) Z_{LRT} , (b) Z_{CP} , (c) Z_{PV} , and (d) Z_{380K} .

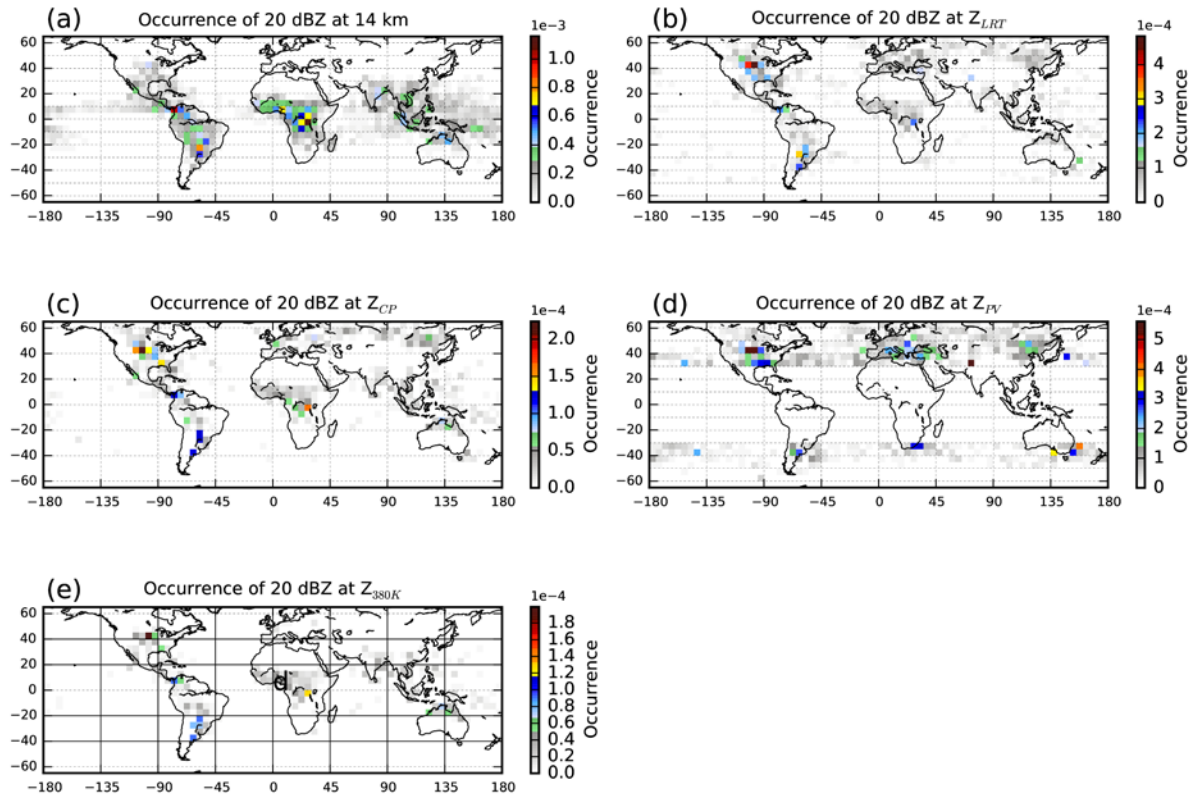


Figure 7. Global distribution of occurrence of 20 dBZ at different reference levels. (a) 14 km, (b) Z_{LRT} , (c) Z_{CP} , (d) Z_{PV} , and (e) Z_{380K} . The occurrences are calculated by dividing total number of pixels with 20 dBZ at reference levels with total number of sampled pixels in each $5^\circ \times 5^\circ$ box.

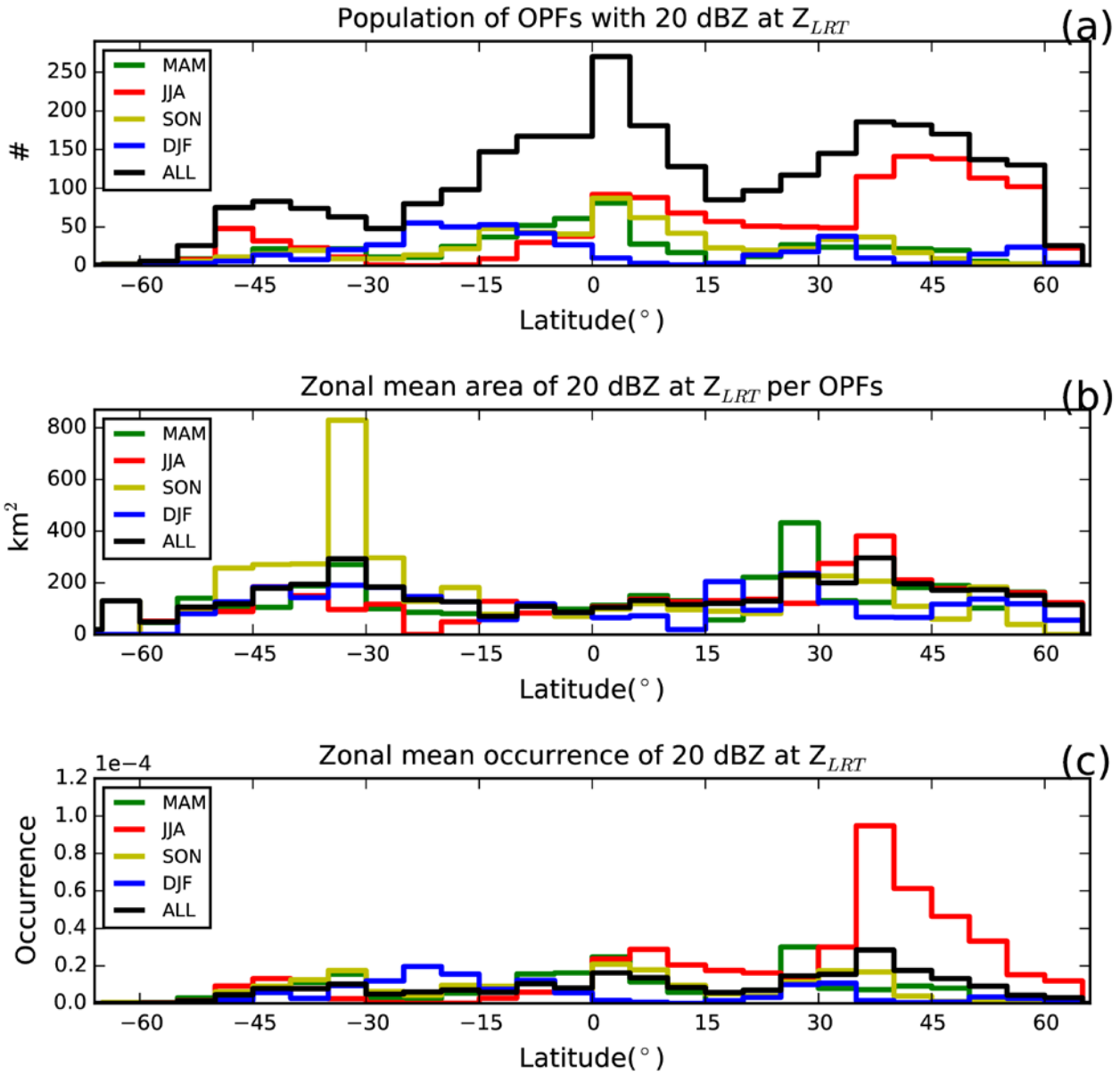


Figure 8. (a) Zonal distribution of populations of OPFs with 20 dBZ at ZLRT. (b) Zonal mean area of 20 dBZ at ZLRT per OPF. (c) Zonal mean occurrence of 20 dBZ at ZLRT. The occurrence in each 5 $^{\circ}$ zones are calculated by dividing 20 dBZ pixels at tropopause with total sampled pixels.

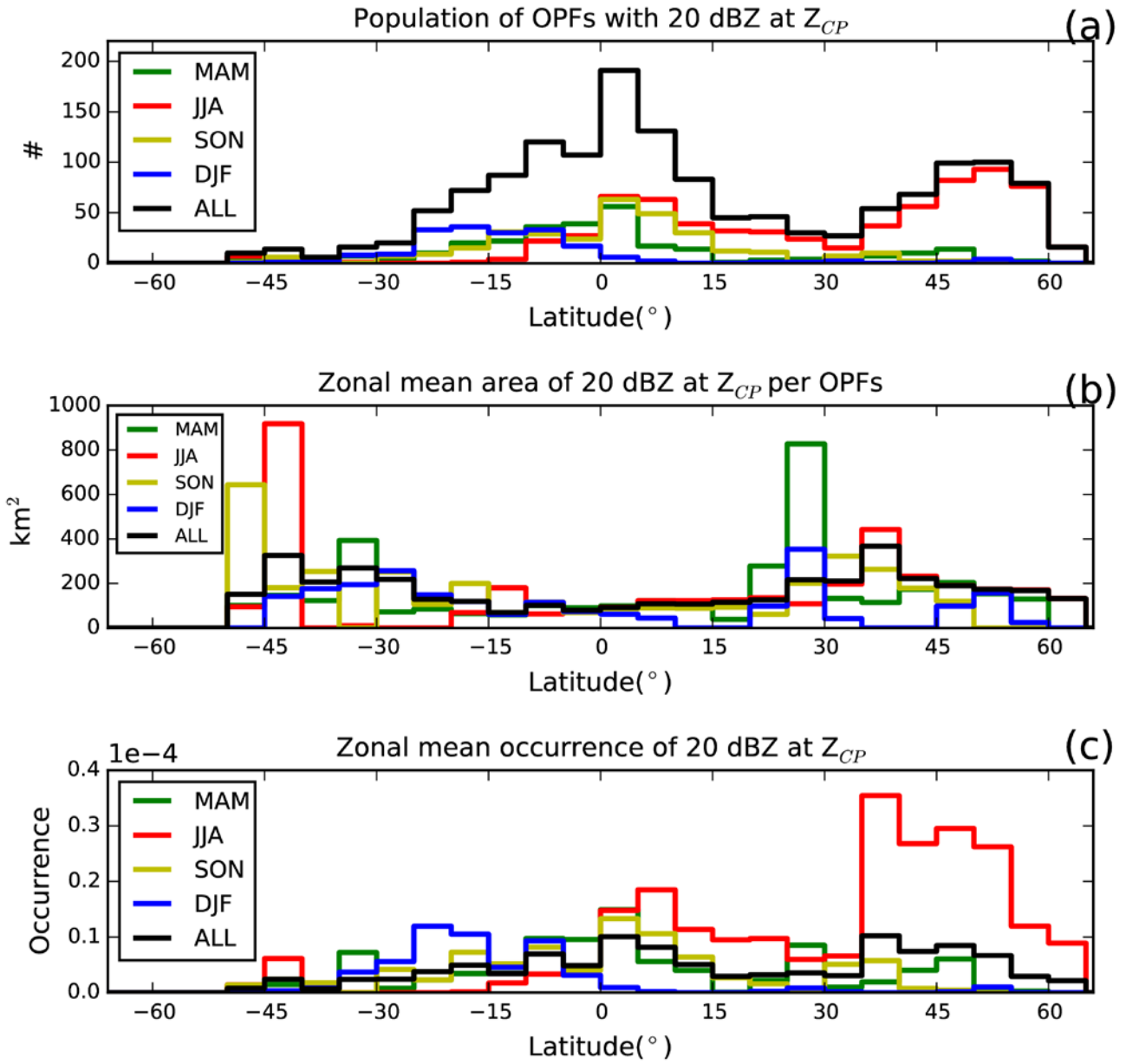


Figure 9. Same as Figure 8, but using Z_{CP} as the reference height.

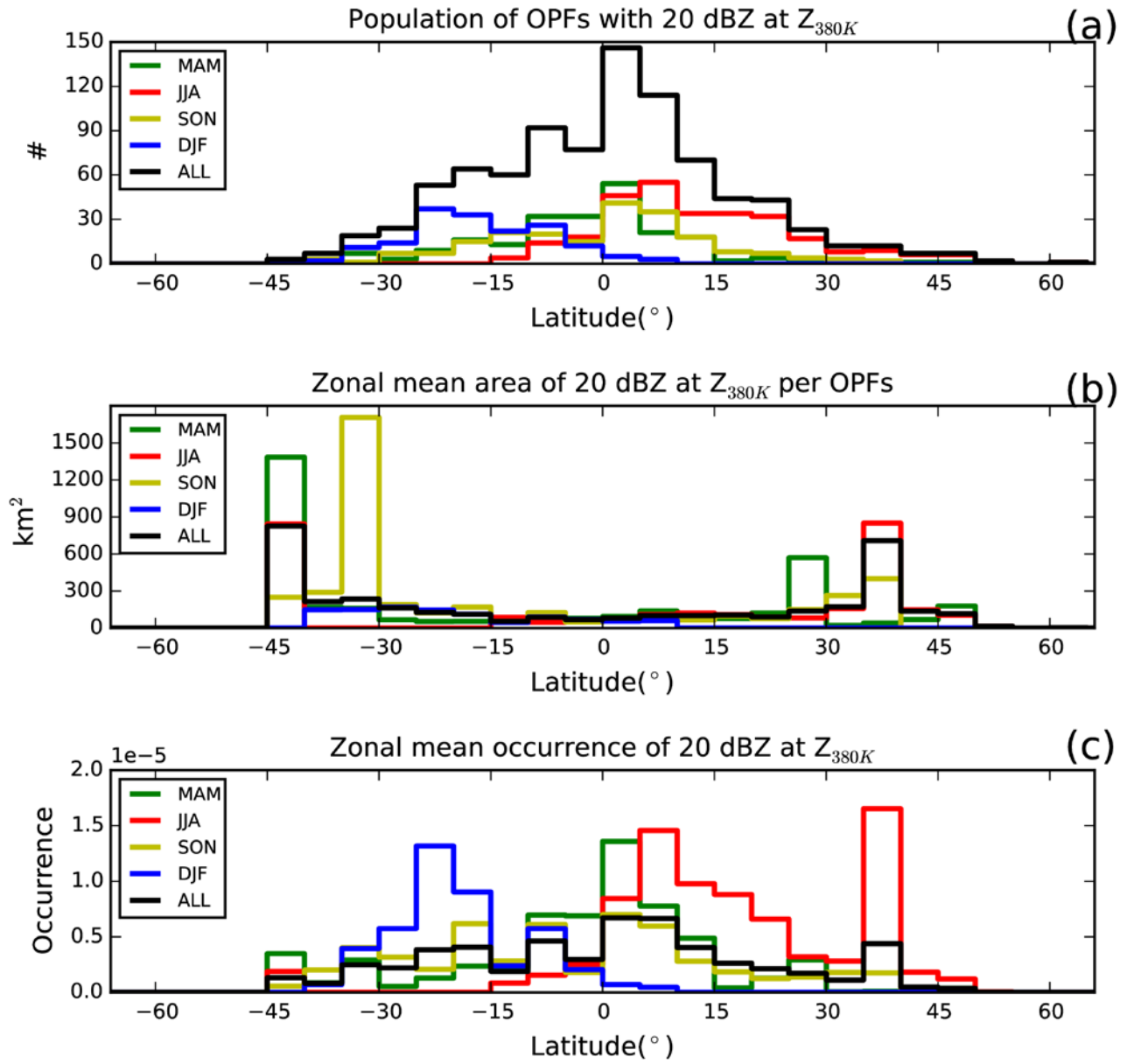


Figure 10. Same as Figure 8, but using Z_{380K} as the reference height.

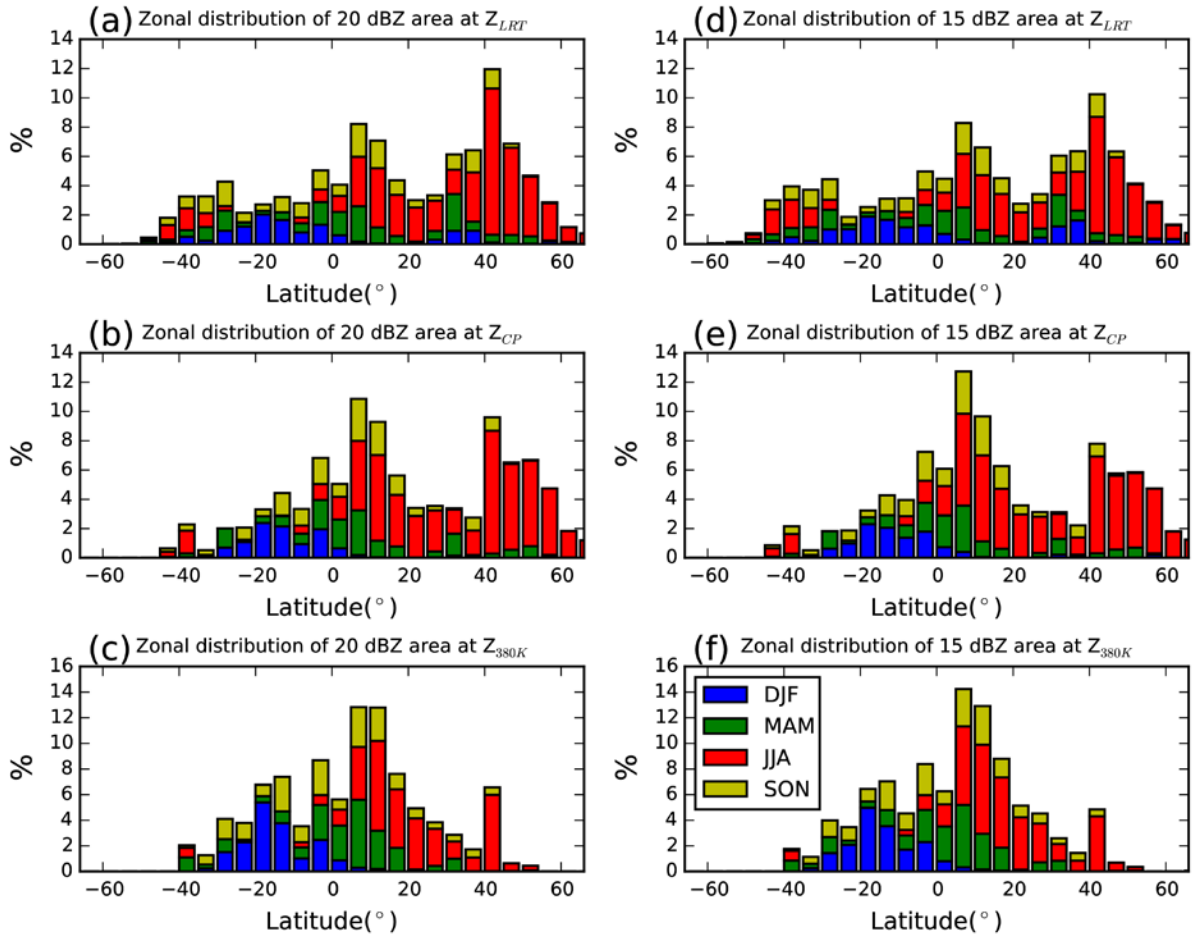


Figure 11. Contribution of areas of 20 and 15 dBZ at Z_{LRT}, Z_{CP}, and Z_{380K} (in units %) in different seasons and latitudes after considering the Earth surface area at each latitude bin. Total values in each panel add up to 100%.

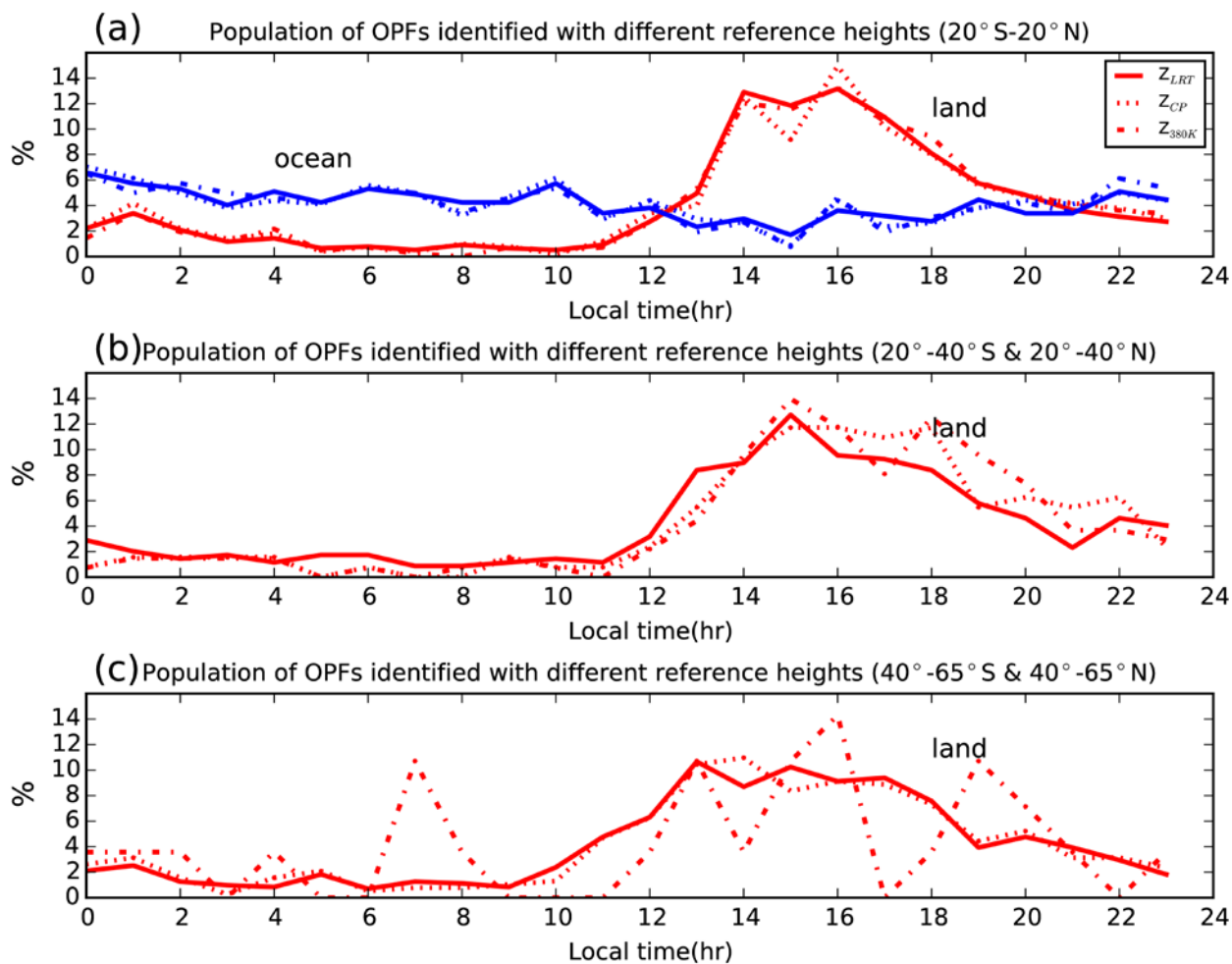


Figure 12. Diurnal variation of population of overshooting precipitation features defined with different reference heights over land (red) and ocean (blue). (a) over 20°S-20°N. (b) over 20°S-40°S and 20°N-40°N. (c) over 40°S-65°S and 40°N-65°N.

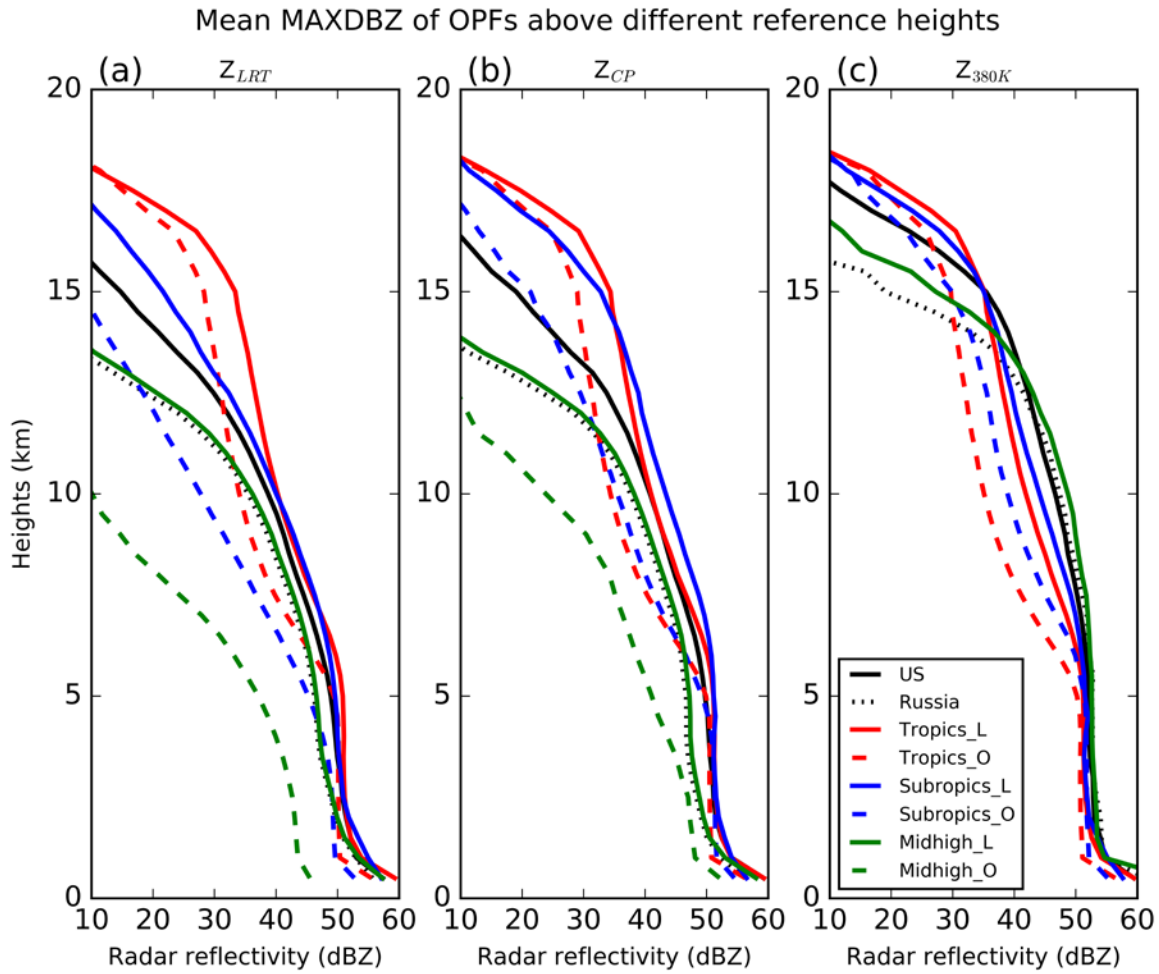


Figure 13. Mean profiles of maximum reflectivity (dBZ) for OPFs above different reference heights in different regions. (a) above Z_{LRT} , (b) above Z_{CP} , (c) above Z_{380K} . The tropics are defined from 20°S - 20°N ; the subtropics are from 20 - 40° ; the midhigh are defined from 40 - 60° ; the region for US is 25 - 60°N and 60 - 120°W ; the region for Russia is 40 - 60°N and 0 - 135°E .

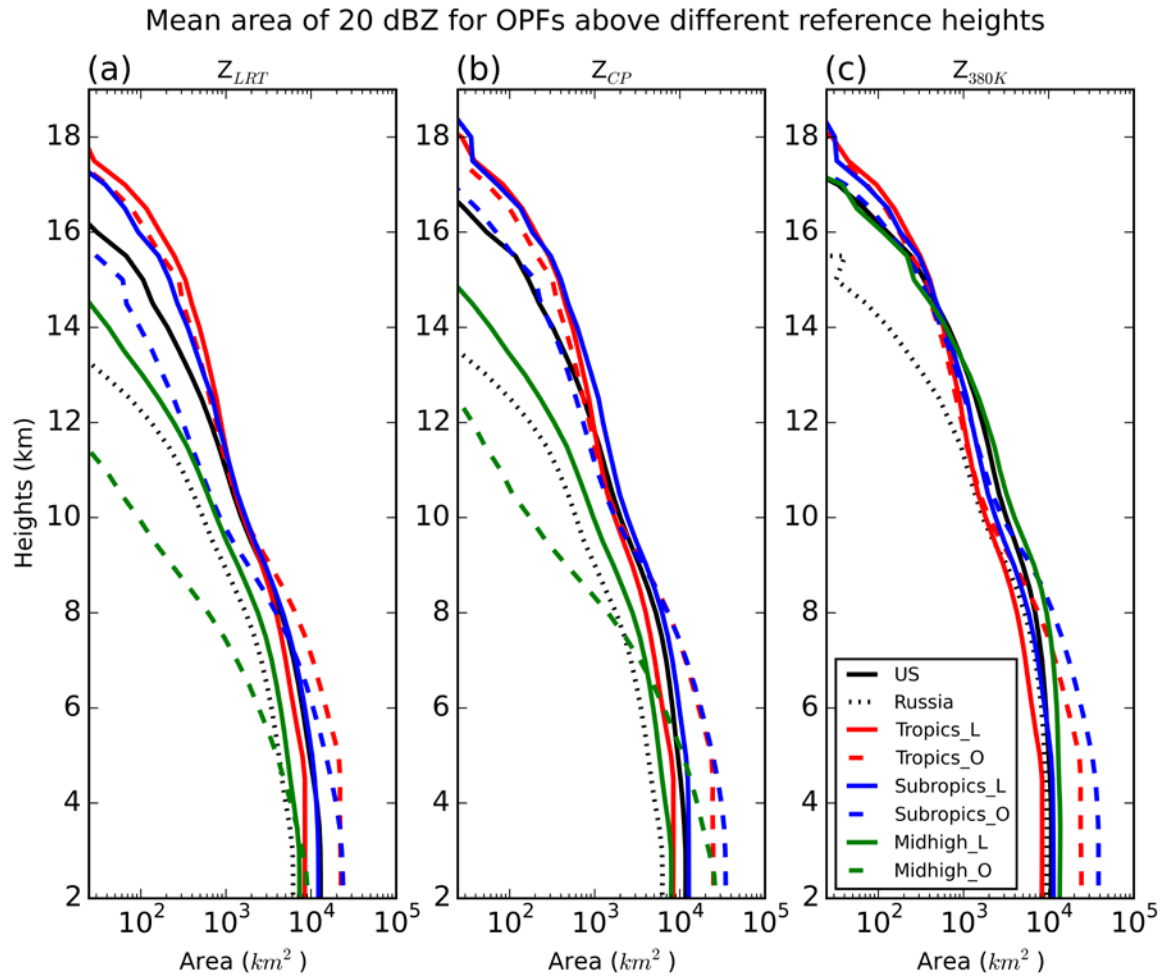


Figure 14. Mean area of 20 dBZ for OPFs above different reference heights in different regions. The region is the same as Figure 13.

Mean area of 30 dBZ for OPFs above different reference heights

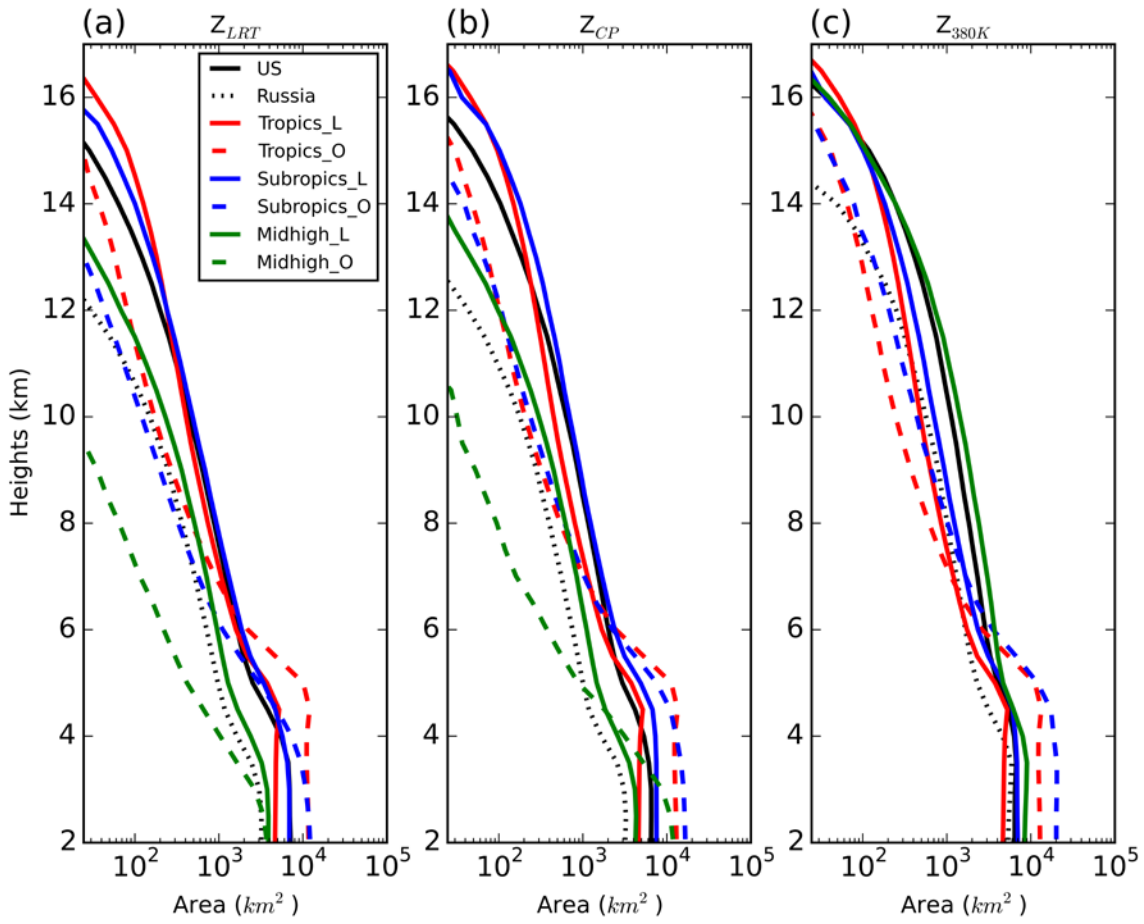


Figure 15. Mean area of 30 dBZ for OPFs above different reference heights in different regions.

Mean area of 40 dBZ for OPFs above different reference heights

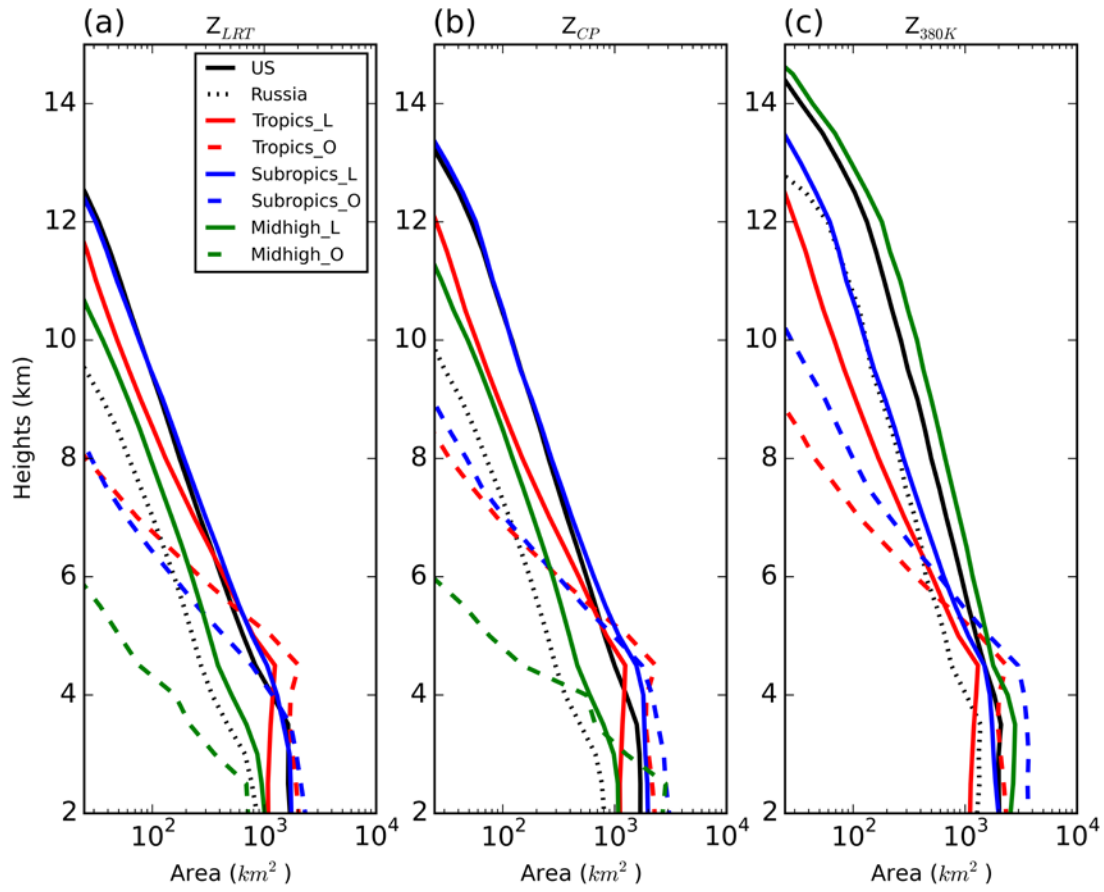


Figure 16. Mean area of 40 dBZ for OPFs above different reference heights in different regions.

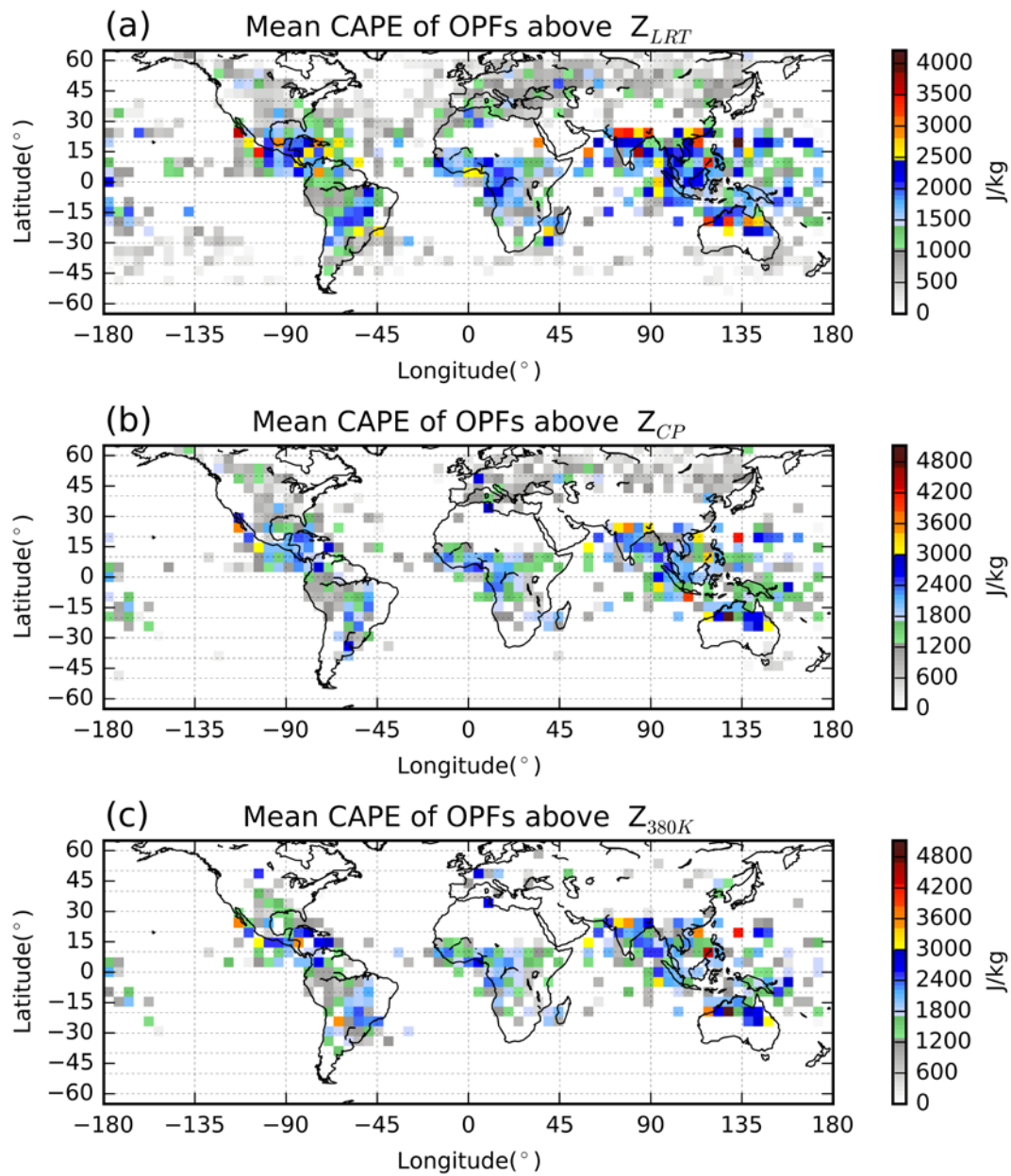


Figure 17. Global distribution of mean CAPE in OPFs at different reference levels. (a) Z_{LRT} , (b) Z_{CP} , and (c) Z_{380K} .

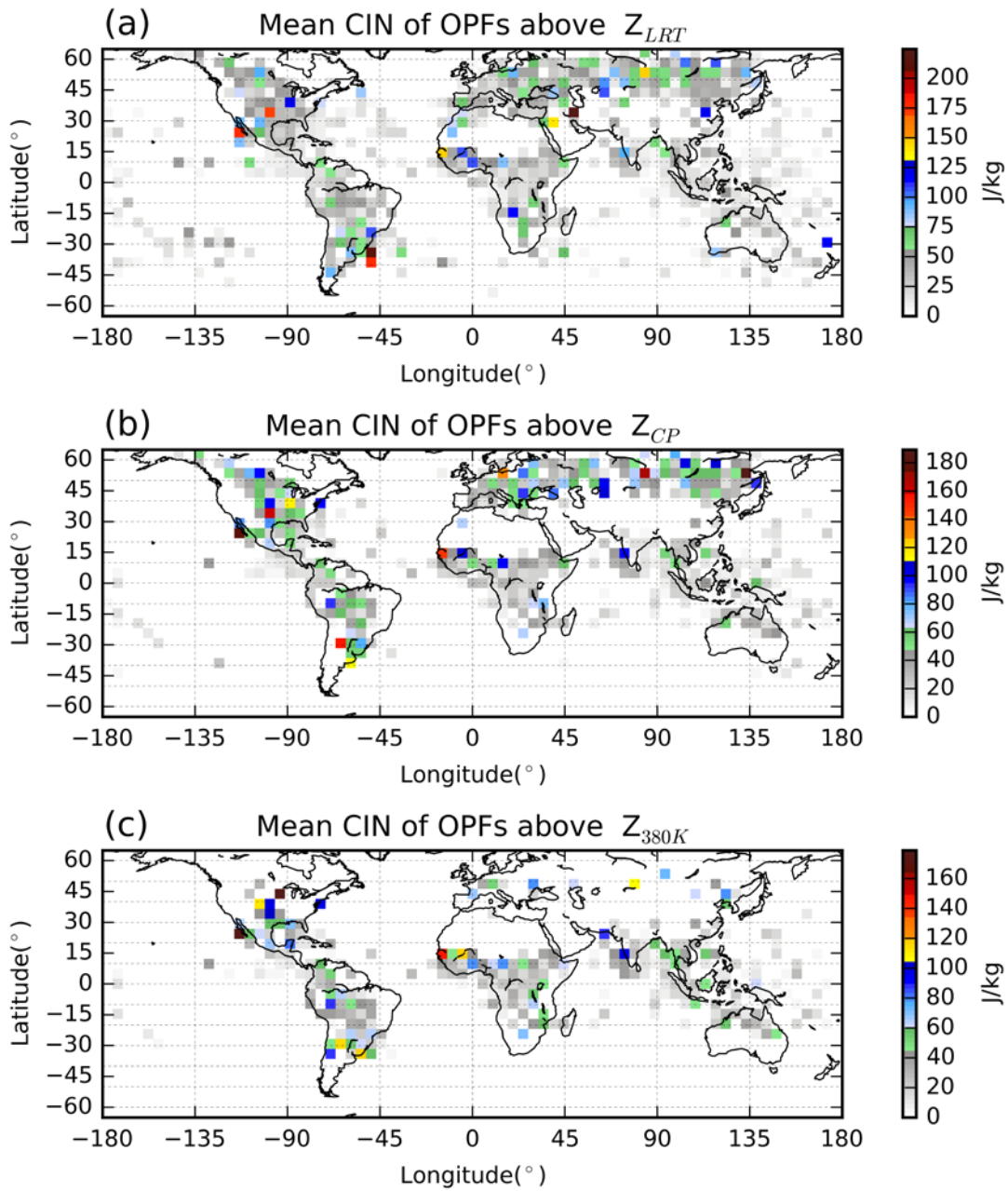


Figure 18. Global distribution of mean CIN in OPFs at different reference levels. (a) Z_{LRT} , (b) Z_{CP} , and (c) Z_{380K} .

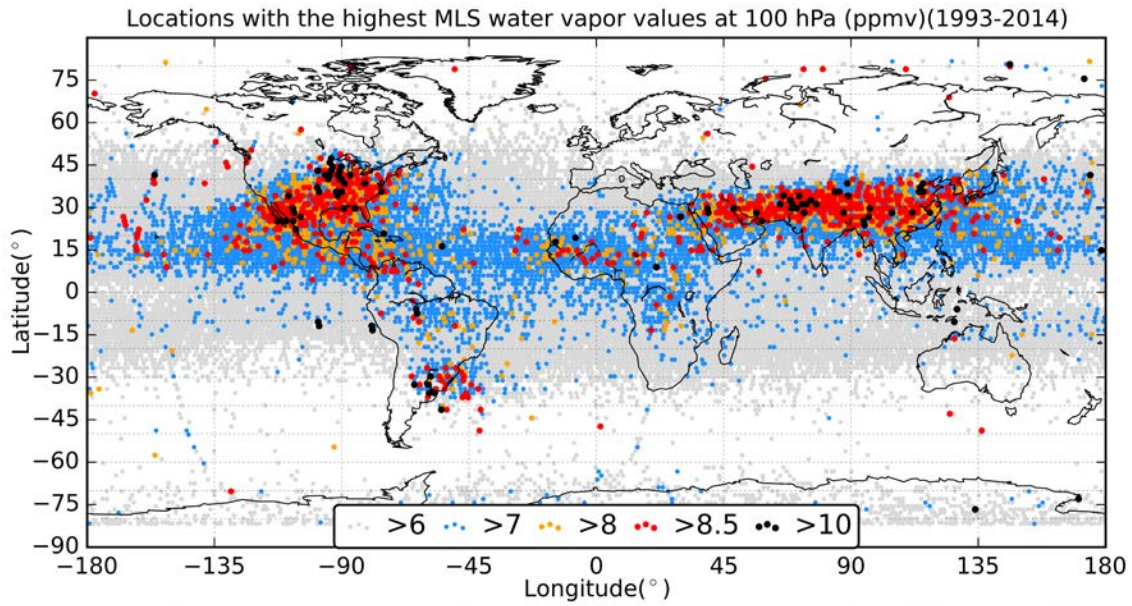


Figure 19. Geographical distribution of highest MLS water vapor values (ppmv) at 100 hPa. The MLS water vapor values categorized by the different numbers are shown in symbols of different colors.

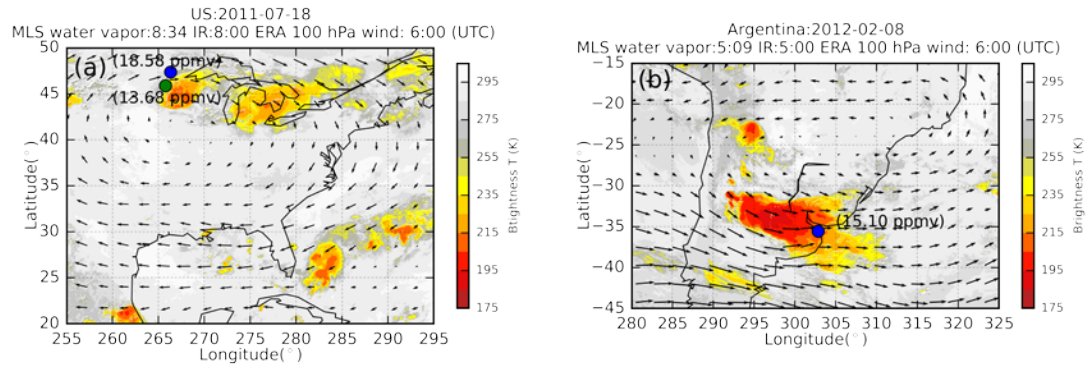


Figure 20. Cases for high MLS water vapor value and their meteorology environmental in different regions. (a) US, (b) Argentina. The time and levels for different dataset are shown in the title.